Convection self-aggregation in CNRM-CM6-1: equilibrium and transition sensitivity to surface temperature

David Coppin[1] and Romain Roehrig[2]

[1]CNRM
[2]CNRM, Université de Toulouse, Météo-France, CNRS

November 24, 2022

Abstract

This study investigates the spontaneous self-aggregation of convection in non-rotating Radiative-Convective Equilibrium (RCE) simulations performed by the CNRM-CM6-1 General Circulation Model within the framework of the RCE Model Intercomparison Project (RCEMIP). In this model, the level of convection self-aggregation at equilibrium, as quantified by metrics based on moisture or moist static energy, strongly increases with sea surface temperature (SST). As it gets warmer, the troposphere gets drier, high cloud cover diminishes in dry regions, the top of high cloud rises and their thickness increases in moist regions, and low cloud cover increases. At high SSTs, the large-scale circulation exhibits a shallow component, stronger than its deep counterpart. The transition towards self-aggregation has a similar first 20-day phase for all SSTs within the 295-305-K range. It primarily involves radiative positive feedback processes. Then, for SSTs above approximately 300 K, a new, slower, transition towards higher levels of self-aggregation occurs. It is concomitant with a shift from a top-heavy to a more bottom-heavy large-scale circulation, a strengthening of the shallow circulation and a reduced mobility of convective aggregates. This second transition is mostly driven by the dry regions, still involves longwave radiative positive feedbacks, but also advective positive feedbacks in the driest regions. It is argued that boundary-layer radiative cooling difference between moist and dry regions, which is stronger at high SSTs, is instrumental in this second phase of self-aggregation. The sensitivity of deep convection to environmental dry air also likely acts as a positive feedback on the system.

Convection self-aggregation in CNRM-CM6-1: equilibrium and transition sensitivity to surface temperature

D. Coppin[1], R. Roehrig[1]

[1]Centre National de Recherches Météorologiques, Université de Toulouse, Météo-France, CNRS, Toulouse, France

Key Points:

- The sensitivity to surface temperature of convective self-aggregation under radiative-convective equilibrium is documented in CNRM-CM6-1
- Increase of self-aggregation with surface temperature is associated to an efficient shallow circulation between dry and moist regions
- A second slower transition towards self-aggregation at high surface temperature is primarily driven by radiative processes in dry regions

Corresponding author: Romain Roehrig, `romain.roehrig@meteo.fr`

Abstract

This study investigates the spontaneous self-aggregation of convection in non-rotating Radiative-Convective Equilibrium (RCE) simulations performed by the CNRM-CM6-1 General Circulation Model within the framework of the RCE Model Intercomparison Project (RCEMIP). In this model, the level of convection self-aggregation at equilibrium, as quantified by metrics based on moisture or moist static energy, strongly increases with sea surface temperature (SST). As it gets warmer, the troposphere gets drier, high cloud cover diminishes in dry regions, the top of high cloud rises and their thickness increases in moist regions, and low cloud cover increases. At high SSTs, the large-scale circulation exhibits a shallow component, stronger than its deep counterpart. The transition towards self-aggregation has a similar first 20-day phase for all SSTs within the 295–305-K range. It primarily involves radiative positive feedback processes. Then, for SSTs above approximately 300 K, a new, slower, transition towards higher levels of self-aggregation occurs. It is concomitant with a shift from a top-heavy to a more bottom-heavy large-scale circulation, a strengthening of the shallow circulation and a reduced mobility of convective aggregates. This second transition is mostly driven by the dry regions, still involves longwave radiative positive feedbacks, but also advective positive feedbacks in the driest regions. It is argued that boundary-layer radiative cooling difference between moist and dry regions, which is stronger at high SSTs, is instrumental in this second phase of self-aggregation. The sensitivity of deep convection to environmental dry air also likely acts as a positive feedback on the system.

Plain Language Summary

In idealized configurations of the Earth, convective clouds can spontaneously organize into large clusters: this is convective self-aggregation. We investigate the sensitivity of this process to surface temperature in the atmospheric component of the state-of-the-art global climate model CNRM-CM6-1. For surface temperatures spanning a typical range of tropical conditions (295–305 K), the model exhibits an aggregated state when equilibrium is reached. As the surface gets warmer, convection is more aggregated, the troposphere gets drier, high clouds get less frequent in dry regions and low cloud cover increases. When starting from homogeneous conditions, an initial rapid phase of self-aggregation occurs in all experimented SST. Radiative processes are instrumental in leading to self-aggregation. For warm surface temperature above approximately 300 K, a second, slower,

transition occurs and leads to higher levels of self-aggregation. It is associated with an adjustment of the large-scale circulation, in which shallow circulations in the lower troposphere (surface-700 hPa) and between dry and moist regions strengthens. The radiative loss of energy within the boundary layer, and its unbalanced state between dry and moist regions after the initial transition is argued to the main process at play.

1 Introduction

Tropical deep convection organizes across a wide range of scales, driven by a variety of physical processes. It can be forced by equatorial waves (Kiladis et al., 2009), topography or surface temperature gradients, either above ocean (Shamekh et al., 2020a), land (Becker & Stevens, 2014; Hohenegger & Stevens, 2018) or at the boundaries between both types of surface (Coppin & Bellon, 2019a, 2019b). At mesoscale, convection is able to generate its own sources of organization as is the case for Mesoscale Convective Systems (Houze, 2004) or squall lines (Rotunno et al., 1988). At larger scales, large convective envelopes such as the Madden-Julian Oscillation (Madden & Julian, 1994) or various forms of organization along the equator are also able to modify the average zonal or meridional circulations (Bellenger et al., 2009).

One type of organization that arises in idealized numerical simulations, such as under the Radiative-Convective Equilibrium (RCE) hypothesis, is self-aggregation (e.g., Wing, 2019). This spontaneous organization of deep convection has been studied in a wide range of models, from small-domain large-eddy or cloud-permitting simulations (Bretherton et al., 2005; Muller & Held, 2012; Tompkins & Semie, 2017) to global, Earth-scale simulations with general circulation models (GCM – Popke et al., 2013; Coppin & Bony, 2015; Becker et al., 2017), and under a wide range of surface boundary conditions: from fixed and uniform surface temperature (Khairoutdinov & Emanuel, 2013; Wing & Emanuel, 2014; Cronin & Wing, 2017) to an interactive surface, based on an ocean mixed-layer model (Coppin & Bony, 2017, 2018; Shamekh et al., 2020b). These models share the same drying of the free troposphere as convection aggregates and the subsequent increase in outgoing longwave radiation to space (Bretherton et al., 2005; Holloway et al., 2017; Wing et al., 2017). This atmospheric response to convective aggregation is also consistent with observations (Tobin et al., 2012, 2013; Stein et al., 2017). In contrast, models do not agree on the sensitivity of aggregation to sea surface temperature (SST) nor on the details of the various mechanisms controlling the initiation, maintenance or inhibition of convective aggregation. For example, in contrast to Cloud Permitting Models (CPM), aggregation almost always increases with SST in GCMs (Becker & Wing, 2020). Such a difference critically limits our ability to understand and quantify the impact of convective aggregation on the climate system. Therefore efforts to better characterize the robustness and dependency of self-aggregation to the surface temperature and to better understand the underlying mechanisms recently culminated in the RCE Model Intercomparison Project (RCEMIP, Wing et al., 2018): using a coordinated setup of RCE simulations, RCEMIP aims at clarify the discrepancies between CPMs and GCMs, as well as among the numerous GCMs that took part in the exercise.

Even though the mechanisms leading to self-aggregation differ among models, most of them indicate that feedbacks between longwave (LW) radiation, water vapor and clouds (Bretherton et al., 2005; Muller & Held, 2012; Craig & Mack, 2013; Wing & Emanuel, 2014; Coppin & Bony, 2015) favors the initiation and maintenance of self-aggregation while the surface flux feedback alternates from being positive in the early stages to being negative later on (Tompkins & Craig, 1998; Wing & Emanuel, 2014; Coppin & Bony, 2015; Holloway & Woolnough, 2016; Wing & Cronin, 2016). Other identified processes appear more model-dependent: the relative importance of clear- versus cloudy-sky radiative processes, the relative contribution of direct (diabatic) or indirect (i.e. through the atmospheric circulation) radiative effects in the evolution of convective aggregation, the role of moist static energy (MSE) horizontal advection and the role of the shallow circulation that develops in a number of CPM simulations between convectively-active and convectively-suppressed regions (Muller & Bony, 2015; Shamekh et al., 2020b).

The latter point has been the focus of several studies pointing out the crucial role of either the free troposphere or the boundary layer (BL) in the establishment of this shallow circulation and its potential role in the initiation of convective self-aggregation. Bretherton et al. (2005) find that enhanced radiative cooling in the lower troposphere of the dry regions leads to the formation of a shallow circulation transporting MSE up-gradient, from low-MSE to already high-MSE regions, thereby favoring self-aggregation through the increase of MSE gradients and the MSE variance. This has been confirmed by several CPM studies, although the nature of the radiative feedbacks driving this shallow circulation depends on the model and its configuration. Muller and Bony (2015) suggest that the BL differential radiative cooling rate between dry and moist regions is the main driver. The BL-centric framework of Yang (2018) confirms the key role of BL diabatic processes and further suggests that an additional buoyancy effect is necessary to establish a horizontal pressure gradient able to drive convective self-aggregation. This hypothesis has been verified by conceptual bulk models for both the dry and moist BL structures (Naumann et al., 2017, 2019), which show that heterogeneous radiative BL cooling is able to produce pressure gradients between areas of strong and weak BL cooling. The strength of the induced shallow circulation is comparable to that caused by surface temperature differences of a few kelvins, emphasizing the potential first-order effect of spatial differences in BL radiative cooling for self-aggregation.

The strength of the shallow circulation has also been linked to the speed of self-aggregation. Using a CPM coupled with interactive SSTs, Shamekh et al. (2020b) underline that larger surface pressure anomalies, which result from both BL radiative cooling and positive SST anomalies in the dry regions, strongly modulate how fast convection self-aggregates. But, in these simulations with interactive SSTs as well as in those more commonly using fixed SSTs, the larger radiative cooling in the BL and lower troposphere strongly depends on the free-tropospheric drying induced by the large-scale deep circulation that emerges with self-aggregation. The respective role and balance between these two circulations in convective self-aggregation remains unclear, as well as how this balance can shift with surface warming. The existence and role of such BL differential radiative cooling and associated shallow circulation has yet to be shown in GCMs.

In this paper, we document and investigate the mechanisms responsible for convection self-aggregation in the CNRM-CM6-1 GCM (Voldoire et al., 2019; Roehrig et al., 2020). This analysis thus focuses on the equilibrium states reached by the model under various SSTs, but also on the paths taken by the model to aggregate convection. For some SSTs, the path involves multiple phases of self-aggregation, with different timescales. After describing the CNRM-CM6-1 model, the experiments performed with it and the diagnostics used to study self-aggregation in Section 2, we investigate the equilibrium states of the model in Section 3. In particular we assess whether different metrics characterizing self-aggregation consistently evolve with increasing SST. Section 4 then investigates the transient response and the feedbacks driving the different phases of convection self-aggregation. Section 5 summarizes and discusses our main findings.

2 Methods

2.1 The CNRM-CM6-1 atmospheric component

We use the atmospheric component of the CNRM-CM6-1 climate model (Voldoire et al., 2019), namely the global atmospheric model ARPEGE-Climat 6.3 (Roehrig et al., 2020). This model version contributed to the RCEMIP initiative (Wing et al., 2018, 2020).

ARPEGE-Climat is a spectral model derived from cycle 37 of the ARPEGE/IFS (Integrated Forecast System) numerical weather prediction model developed jointly by Météo-France and the European Center for Medium-range Weather Forecast. It uses a linear triangular truncation T127 with a corresponding reduced Gaussian grid (Hortal & Simmons, 1991). The model horizontal resolution is about 1.4°. Along the vertical the model encompasses 91 vertical levels, following a progressive hybrid σ-pressure coordinate. The first and last model levels are near 10 m and 80 km, respectively, and the vertical resolution ranges from 20 to 200 m in the boundary layer, while being around 400–500 m in the free troposphere.

The dynamical core is based on a two-time level semi-Lagrangian numerical integration scheme. It resolves the vorticity and divergence form of the primitive equations, with temperature and surface pressure logarithm being the thermodynamic state variables. It also computes the advection of specific humidity and eight microphysical species (four for the large-scale microphysics scheme, four for the convection scheme). Horizontal diffusion, which intensity depends on the wave length, the altitude and the diffused variable, is used to stabilize the model and allows, together with the semi-Lagrangian scheme, to keep rather long model time steps (15 minutes).

Longwave radiation calculations follow the GCM version of the Rapid Radiation Transfer Model (Mlawer et al., 1997) while the shortwave radiation calculations are based on the six-band scheme of Fouquart and Bonnel (1980) and Morcrette et al. (2008). The stratiform microphysics scheme treats cloud liquid water, cloud ice crystals, rain and snow, and accounts for autoconversion, sedimentation, icing-melting, precipitation evaporation, and collection processes (Lopez, 2002). The turbulence is solved by the 1.5-order turbulent kinetic energy scheme of (Cuxart et al., 2000) using the mixing length of Bougeault and Lacarrere (1989). Finally, dry, shallow and deep convection regimes are represented using the unified, bulk, mass-flux framework described in Piriou et al. (2018). It follows the ideas of Gueremy (2011) for the convective profile and closure, and those of Piriou et al. (2007) for an explicit separation between the convective vertical transport and the convective microphysical processes. The convective microphysical processes are thus treated in the same way as the large-scale, resolved microphysical processes (Lopez, 2002), considering only that they occur in the convective environment. As a result, convective microphysical species mirror those in the convection environment, thereby allowing entrainment and detrainment of the condensates. Entrainment and detrainment processes depend on the prognostic updraft vertical velocity and follow the buoyancy sorting approach of Bretherton et al. (2004). The scheme closure is based on the relaxation of the dilute Convective Available Potential Energy.

2.2 RCEMIP simulations

CNRM-CM6-1 is run in the RCE configuration without rotation, following RCEMIP guidelines (Wing et al., 2018): fixed and uniform SSTs of 295 K, 300 K and 305 K, constant and uniform incoming solar radiation at the top of atmosphere and zenith angle (551.58 W m^{-2} and 42.05°, respectively). The simulations are uniformly initialized from the equilibrium profiles obtained from single-column experiments with the same model and for the same SSTs. The three CNRM-CM6-1 RCE simulations show different degrees of convection aggregation as emphasized by the patterns of Column Relative Humidity (CRH – ratio of precipitable water to saturated precipitable water) and the aggregation indices indicated in Figure 1 (see also Wing et al., 2020).

Since the timing and strength of convective self-aggregation may depend on the initial state, we designed ensembles of five simulations for each of the 295-K, 300-K and 305-K SSTs. Each member of the ensemble is initialized with a globally-averaged instantaneous state taken from the equilibrium phase of the first member at the same SST (i.e. the RCEMIP simulation described above). Besides, in order to further investigate the aggregation sensitivity to SSTs, additional experiments are performed at each SST between 295 K and 305 K by increment of 1 K. All the simulations last three years. The equilibrium values are averages over the last year.

2.3 Moist static energy framework

The traditional framework to analyse self-aggregation of deep convection is based on the frozen moist static energy (FMSE), which is conserved under adiabatic processes including the phase change of water. When integrated over the column, its variance increases as convection organizes: the FMSE increases in moist regions and decreases in dry regions. In the CNRM-CM6-1 model, the FMSE h follows the definition of Wing et al. (2018):

$$h = c_p T + gz + L_v q_v - L_f q_i \tag{1}$$

where $\mathrm{c_p}$ denotes the specific heat of moist air, T the temperature, g the gravity acceleration, z the geopotential height, $\mathrm{L_v}$ and $\mathrm{L_f}$ the latent heat of vaporization and fusion at the water triple point, respectively, and $\mathrm{q_v}$ and $\mathrm{q_i}$ the specific humidity and the ice specific mass, respectively (including convective and large-scale components of cloud ice crystal and precipitating snow).

The FMSE range strongly depends on the SST, which renders the comparison of indices or budget based on FMSE difficult for different SSTs. To account for this dependency, we follow Pope et al. (2021) and define the normalized vertically-integrated FMSE $\widehat{h}_n$ between theoretical upper and lower limits using the formula:

$$\widehat{h}_n = \frac{\widehat{h} - \widehat{h}_{\mathrm{min}}}{\widehat{h}_{\mathrm{max}} - \widehat{h}_{\mathrm{min}}} \tag{2}$$

where hats ($\widehat{\ }$) denote a density-weighted vertical integral, and $\widehat{h}_{\mathrm{min}}$ and $\widehat{h}_{\mathrm{max}}$ the lower and upper limits of $\widehat{h}$ for a given SST, respectively. $\widehat{h}_{\mathrm{min}}$ is defined as the vertically-integrated FMSE of a dry adiabatic profile with zero moisture in the troposphere, plus the integrated FMSE of the initial profile above the tropopause. $\widehat{h}_{\mathrm{max}}$ corresponds to the vertically-integrated FMSE of a fully saturated moist pseudo-adiabatic profile from the surface to the tropopause, plus the integrated FMSE of the initial profile above the tropopause. The tropopause is defined as the lowest level in the initial profile at which the lapse rate decreases below 2 K km^{-1}.

To investigate the relative importance of different processes impacting the variance of the normalized vertically-integrated FMSE $\widehat{h}_n$, we use the same budget equation derived from Wing and Emanuel (2014) but replace the vertically-integrated FMSE $\widehat{h}$ by its normalized counterpart (see also Pope et al., 2021):

$$\frac{1}{2}\frac{\partial \widehat{h}_n'^2}{\partial t} = \widehat{h}_n'\mathrm{SEF}_n' + \widehat{h}_n'\mathrm{NetSW}_n' + \widehat{h}_n'\mathrm{NetLW}_n' + \widehat{h}_n'\widehat{\nabla_h \cdot (\mathbf{u}h_n)} \tag{3}$$

with SEF the surface enthalpy flux (sum of sensible and latent heat fluxes), NetSW and NetLW the net atmospheric column shortwave (SW) and longwave radiative heating sources, and $\widehat{\nabla_h \cdot (\mathbf{u}h_n)}$ the vertically-integrated horizontal divergence of the normalized FMSE. Primes ($'$) denote the local anomalies from the instantaneous domain mean. This enables us to better compare the strength of the feedbacks driving self-aggregation for different SSTs.

2.4 Characterization of CRH distributions

The next section compares different aggregation indices used in the literature to characterize convective aggregation. Because they are not based on the same variables and correspond to different visions of what an aggregated atmosphere looks like, these indices often evolve separately with SSTs, or with time for a given SST. In order to better analyze these differences and gain a more detailed view of what exactly is changing in the moisture distribution with self-aggregation, we approximate the CRH spatial probability distribution function (PDF) by either a unique lognormal distribution or, when convection is aggregated, by the superimposition of two such distributions, one for each of the dry and moist modes of CRH. As a result, the CRH distribution, and thereby the aggregated state, can be characterized with 5 parameters. The analytical form of the approximated CRH distribution reads:

$$f(x) = \frac{1-\alpha}{x\sigma_d\sqrt{2\pi}} e^{-\frac{(\ln x - \mu_d)^2}{2\sigma_d^2}} + \frac{\alpha}{x\sigma_m\sqrt{2\pi}} e^{-\frac{(\ln x - \mu_m)^2}{2\sigma_m^2}} \tag{4}$$

with α, the fraction of the total PDF covered by the moist PDF, and μ_d, μ_m, σ_d and σ_m, the expected value (μ) and standard deviation (σ) of the dry and moist lognormal distributions, respectively.

The point where both distributions are equal is called CRH$_c$. It is used to separate dry and moist regions. The best fit for each reconstructed PDF correspond to the combination of the five parameters that minimizes the quadratic error with the original PDF. Examples of optimized fits for several days of the 305-K simulation are shown in Figure S1 (supplemental material).

This decomposition of the CRH spatial distribution provides a solid framework to diagnose how the CRH distribution varies with time or with the SST. Higher expected value μ corresponds to a broader distribution while higher standard deviation σ means the distribution is more skewed towards one of its extremes (e.g., Text S2 and Figure S2). In addition to these parameters, we also estimate the CRH value at the peak of each log-normal distribution (CRH_d and CRH_m for the dry and moist distributions, respectively).

3 Convection self-aggregation equilibrium in CNRM-CM6-1

3.1 Quantifying the level of convection self-aggregation

While convection is mostly organized along bands of high CRH, the main difference between SSTs is the larger dry areas and increasing contrasts at high SSTs (Figure 1). To objectively quantify self-aggregation, a wide range of indices are used in the literature. Figure 2 illustrates some of those that are easily applicable to coarse-resolution GCMs for all the explored SST range as well as for all members of the 295-K, 300-K and 305-K ensembles.

All indices using vertical integrals of variables associated with humidity, i.e. the variances of vertically-integrated FMSE ($\mathrm{var}(\hat{h})$) and normalized FMSE ($\mathrm{var}(\hat{h}_n)$), precipitable water (var(PRW)) and CRH (var(CRH)), show a gradual increase of self-aggregation with warming, with simulations between 298 K and 301 K having a similar equilibrium. Since $\mathrm{var}(\hat{h}_n)$ is well correlated with var(CRH) and var(PRW), and facilitates the comparison of the aggregation mechanisms across SSTs, we now use it as our main index to quantify convective aggregation.

The shallow circulation efficiency η (see appendix A for details) is a dynamical index which quantifies the fraction of mass transport between dry and moist regions done by the shallow circulation (Shamekh et al., 2020b). It is highly correlated with $\mathrm{var}(\hat{h}_n)$. This suggests a direct link between self-aggregation and the strength of the shallow circulation. The variances of normalized FMSE and η are also well correlated with the surface pressure difference between moist and dry regions (Δp_s) and the net radiative boundary-layer warming difference between moist and dry regions ($\Delta \partial_t T|_{\mathrm{rad}}$, positive when radiative cooling is stronger in the dry regions). The latter difference mainly results from differences in the LW clear-sky temperature tendencies (second to last column in Figure 2). This suggests that, as proposed by Naumann et al. (2017) and Naumann et al. (2019), this heterogeneous radiative boundary-layer cooling is consistent with positive surface pressure anomalies in dry regions, which thereby strengthens the shallow circulation. In turn, the latter positively feeds back on self-aggregation as it enhances the FMSE import in moist regions and thus the variance of $\hat{h}_n$.

In contrast to the previous indices, the subsiding fraction (SF), i.e. the fraction of the domain where subsidence occurs at 500 hPa (noted SF500), as well as those fraction computed using the 850-hPa vertical velocity (SF850) or the vertically-averaged vertical velocity ($\overline{\mathrm{SF}}$), increase from 295 K to 298-299 K and then decrease up to 305 K, with a rate depending on the SF index version. This behavior strongly contrasts with the other indices and indicates that a maximum subsiding fraction does not always relate to maximum aggregation as quantified with the $\hat{h}_n$ variance (see also Wing et al., 2020). The rather high sensitivity of the SF indices to the level used in their calculation questions the way self-aggregation should be quantified.

Because of the bi-modal property of the CRH distribution (e.g., Figure S1 – also true for $\hat{h}_n$ or PRW), the use of a variance metric can also be questioned. We therefore explore a more detailed approach to characterize the CRH distribution and its sensitivity to SSTs (Section 2.4).

The weight α of the moist PDF decreases with SST until 298 K and then saturates, with a distinct minimum at 298-299 K (Figure 3). A similar pattern is found for μ_m and CRH_m, further emphasized by the strong correlations between these three parameters. σ_m is also maximum at 298-299 K but decreases back to low-SST levels at higher SST. This underlines that, for SSTs up to 299 K, the moist component of the CRH distribution becomes moister and narrower, while its area decreases. For higher SSTs, the distribution moves back to lower CRH values while maintaining a similar fraction of the full PDF.

In contrast, μ_d and CRH_d decrease with SST and strongly correlate with the normalized FMSE variance $\mathrm{var}(\hat{h}_n)$. Therefore, as SST increases, the dry component of the CRH distribution becomes drier and narrower. This also indicates that the evolution of the dry regions is the primary driver of the monotonic FMSE variance increase with SST (as well as that of the shallow circulation efficiency η), especially above 298-299 K.

The distinct maximum of σ_m at 298-299 K and its relationship with $\mathrm{var}(\hat{h}_n)$ mirrors that between SF indices and $\mathrm{var}(\hat{h}_n)$ in Figure 2. The high correlation of α with μ_m and CRH_m also suggests that the moistest regions partly drive the fraction of the domain covered by subsidence (or large-scale ascent) at equilibrium. The relationship between SF indices and the moist regions is however more complex and SF indices only weakly correlate with μ_m and CRH$_m$ (not shown). This hints that SF indices are not fully controlled by the CRH level in moist regions, which thus does not fully drive the large-scale deep circulation.

To summarize, SF indices and α thus characterize self-aggregation as a balance between moist/convective and dry/subsiding regions and are mainly controlled by the moist component of the CRH distribution and convection, while var($\hat{h}_n$) and η are primarily driven by the shape of the moisture distribution, especially its dry component.

3.2 Atmospheric vertical structure at equilibrium

Convective self-aggregation is generally associated with a drier free troposphere (Bretherton et al., 2005; Tobin et al., 2012, 2013; Stein et al., 2017). This is true in CNRM-CM6-1, particularly in the lower free troposphere, below 650 hPa, where relative humidity (RH) decreases gradually with SST (Figure 4a). This decrease is primarily driven by the dry regions (Figure S3).

The structure of this dry free troposphere varies with SST, from having a single minimum around 500 hPa at 295 K to having a mostly uniform RH profile with two local mimima at 800 hPa and 300 hPa at 305 K. The cloud fraction also gradually decreases with SST between 850 hPa and 300 hPa (Figures 4b and 5). In contrast, the low-level cloud fraction increases with SST, mainly in the dry regions (Figure S3), with a slight downward shift from 298 K on.

In the upper troposphere, as expected from thermodynamical considerations (Hartmann & Larson, 2002; Bony et al., 2016), high clouds rise with increasing SST. The high-cloud fraction decreases from 295 K to 298 K, and then increases from 298 K to 305 K, albeit at a slower rate. In moist regions, it increases from 295 K to 298 K, then decrease until 305 K (Figure S4), while in dry regions, it mostly decreases (Figure S3, see also 5). Thus, for high SSTs, the model behavior at global scale contrasts with the high-cloud fraction decrease with SST predicted by the stability-iris effect (Bony et al., 2016). Although the cloud fraction monotonically reduces in dry regions, convective clouds become thicker in moist regions, possibly also more frequent, thereby compensating the iris effect contraction of the anvil-type high clouds.

In terms of large-scale circulation, Figure 5 emphasizes changes from a large area of shallow convection at moderate CRH and a strong lower tropospheric subsidence at low CRH (Figure 5a) to an extended yet weaker subsidence area in the lower troposphere at moderate CRH, near layers with high low-cloud fractions (Figure 5d). In the moistest region, the circulation evolves from top-heavy to mid- or bottom-heavy ascents, consistently with the enhancement of the shallow circulation between dry and moist regions.

4 Mechanisms leading to convection self-aggregation

Whatever the SST, a first phase of convection self-aggregation occurs during the first 20 days of the simulations (Figure 6a). For SST above approximately 300 K, a second phase of self-aggregation involves longer timescales, from about 100 days at 305 K to 400 days at 300 K. We first focus on the first phase of self-aggregation, common to all the SSTs explored in the present work.

4.1 First phase of convection self-aggregation

The mechanisms driving the first phase of self-aggregation are investigated using the budget of the $\hat{h}_n$ variance (Equation 3) to highlight the involved feedbacks (Figure 7, see also Figure S5 for the separation between clear- and cloudy-sky feedbacks).

At all SSTs, the initial self-aggregation is driven by the LW cloud feedback, with an additional contribution, yet weaker from the latent heat flux feedback. The latter decreases with SST and, after a few days, becomes negative. The SW and LW clear-sky feedbacks also contribute to enhance self-aggregation, though with a slight delay. The amplitude of the surface flux and SW feedbacks is larger at 295 K and 300 K than at 305 K, which likely explains why convection self-aggregates slightly faster at these SSTs. The sensible heat flux feedback is always positive and weak, and slightly larger at low SSTs. Finally, the advection feedback is always negative, except around day 10 at 305 K. Its intensity slightly increases with SSTs. Though the feedback amplitude varies with SSTs, their time evolution over the first 20 days and their relative contribution are mostly similar across SSTs. Therefore, we investigate hereafter the 295-K simulation in more detail to identify the regions where the feedbacks are the most active (Figure 8). Similar diagnostics for 300 K and 305 K are provided in Figures S6 and S7.

Following 2-3 days of spin-up, convection rapidly self-aggregates between days 5 and 10 (black line on Figure 8). The diabatic feedback, dominated by the cloudy-sky longwave feedback, is maximum in the dry regions (Figures 8c and S8). The shortwave (mostly its clear-sky component, see Figure S8) and the surface flux feedbacks in the dry regions also weakly contributes when self-aggregation starts. In contrast, the advection feedback is mostly negative, except in the driest and moistest regions.

This first phase results in a rapid initial drying visible in CRH and precipitable water (black lines in Figure 9a,e, respectively) and the apparition of a relatively low proportion of very dry columns.

At 295 K, the CRH distribution stops evolving after the first 15 days. For SSTs above approximately 300 K, a second phase of self aggregation occurs. The CRH distribution becomes fully bi-modal as the proportion of dry columns increases and becomes similar to or larger than that of their moist counterpart.

4.2 Second phase of convection self-aggregation

When it exists, the second phase of self-aggregation, which ends when the simulation reaches its final equilibrium given in Figure 2, involves much longer timescales than the first phase of self-aggregation (Figure 6). It is characterized by the progressive drying of the free troposphere (Figure 10a-d), particularly in the dry regions (not shown).

The second phase of aggregation consists in a first period when aggregation indices remain approximately constant (Figure 6). It is shorter at high SSTs. It is followed by a second period during which self-aggregation accelerates until its final equilibrium. This acceleration is more pronounced at high SSTs. At the same time, the moist region weight α in the CRH distribution decreases rapidly, σ_d increases, σ_m remains approximately constant and μ_m and μ_d both decrease (Figures 6d,h-k). Thus the dry component of the CRH distribution weights more and gets more skewed towards drier regimes, while its moist component concentrates more around high CRH, getting only slightly moister (see also Figure 9a-d).

We now focus on the 305-K simulation where the increase in aggregation speeds up around days 50-70 (Figure 6) and compare it with the 295 K simulation where this transition phase is absent. Results are similar for SSTs above 300 K, except that the transition takes more time (up to 400 days for 300 K). The early time of the transition in the 305-K simulation (days 20-50) is characterized by adjustments within the low and mid free troposphere, which reduces the geopotential disequilibrium between the moist and dry regions achieved after the first phase of self aggregation (Figure 6e-f). These adjustments in the 305-K simulation are not continuous and involves transient events with timescales of a few days. It also weakly impacts the CRH distribution (Figure 6d,h-k).

Then, from day 50, σ_d sharply increases, μ_d (and CRH$_d$, not shown) sharply decreases, while μ_m decreases at a much more slower pace. This emphasizes the driving role of the dry regions in initiating the second self-aggregation phase. The delayed increase of precipitable water in the moist regions is also consistent (Figure 9h). The transition is concomitant with the slow strengthening of the shallow circulation, which becomes as intense as the deep circulation near day 70 ($\eta = 0.5$, Figure 6b). This change in the large-scale overturning circulation is further illustrated in Figure 11 in a CRH rank-altitude diagram (following Bretherton et al., 2005, see appendix A for the streamfunction computation). Compared to 295 K where the streamfunction is maximum in the upper troposphere and does not vary after the initial 20-day self-aggregation, the streamfunction at 305 K evolves from a top-heavy circulation, similar to that at 295 K, albeit weaker, to a more bottom-heavy circulation, especially after 150 days. The shallow circulation is clearly visible, mostly confined near the margins of moist convective regions. At 295 K, a shallow circulation similarly exists but remains weak compared to the deep one.

The shallow circulation continuously strengthens from day 20 onwards in the 305-K simulation, consistently with the increase of the boundary-layer geopotential height and surface pressure differences between dry and moist regions (Figures 6g,m) and the opposite trend, albeit weaker, in the low and mid troposphere (Figures 6e-f). Around day 60-70, self-aggregation accelerates, at the same time when the shallow circulation efficiency η exceeds 0.5 (Figure 6b), that is when the shallow circulation becomes stronger than its deep counterpart. This is also true at 302 K (around day 150) and 300 K (around day 400), while it clearly does not append at 295 K. The acceleration also coincides with a period of time when moist convective regions become less mobile on average over the globe, with convection suddenly staying over the same area for 10 to 20 days (Figure 6c, see appendix B for the diagnostic computation). The enhanced shallow circulation efficiency is likely able to support a positive net import of FMSE within moist regions thereby favoring their maintenance at the same location for longer time periods (e.g., Raymond et al., 2009).

4.3 Feedback analysis of the second self-aggregation phase

To further understand the processes at play during the second phase of self-aggregation, we now analyze the feedbacks involved in the $\hat{h}_n$ variance budget at 305 K (Figures 12 and 13). Similar results, but with different timings, are found for SSTs above 300 K (e.g., Figure S9 for 302 K).

After the initial phase of self-aggregation, most feedbacks do not evolve much, especially between day 20 and day 50. Then, from day 60, while the feedback magnitudes remain similar, except for the advection feedback, the CRH ranks they impact vary. The LW radiation positive feedback, which remains the dominant positive feedback, mostly occur in moderately-dry CRH columns, thus close to the margins of the moist convectively-active regions. It also remain significant, yet weaker, in the driest regions. This LW feedback is mainly driven by its cloudy-sky component (Figure 13b,e). In contrast, the SW (mostly its clear-sky component), sensible heat flux and latent heat flux feedbacks do not evolve much over the second phase period (Figures 12b,d-e and 13a,d).

Finally, the advection feedback is strongly modified during the self-aggregation acceleration. From day 60, it becomes positive in the driest columns, significantly impacting at day 110 about one third of the domain. There, its positive vertical component dominates its negative horizontal counterpart (Figures 13c,f). The opposite occurs in the transition zone between dry and moist regions (around the grey line on Figures 12 and 13), where the negative horizontal advection feedback dominates. On average over the whole domain, the advection feedback is weak, which thus allows the positive LW feedback to enhance self-aggregation during this second phase. This contrasts with what occurs during the first 60 days, when the vertical and horizontal advection feedbacks are mostly collocated: the total advection feedback is significantly negative and can partly counterbalance the positive LW feedback. The adjustment of the circulation thus drives a spatial decoupling between the deep and shallow circulations, which is key to weaken globally the negative advection feedback and constrain its negative values to remain close to the moist regions. This thereby allows the positive LW feedback to further increase self-aggregation. In the dry regions, the positive vertical advection feedback further enhance self-aggregation, most probably through the further drying of the atmospheric columns (see also Figure 9).

4.4 Sensitivity of the second self-aggregation phase processes to SST

The previous sections suggest an important role of the shallow circulation strengthening during the second self-aggregation phase. Therefore, we now analyze the potential temperature budget contrast between dry and moist regions, to better understand which process might explain its sensitivity to SST. Figures 14 and 15 show the detail of the potential temperature budget in dry and moist regions, respectively, as a function of the degree of self-aggregation (variance of $\hat{h}_n$), for the 295-K, 300-K, 302-K and 305-K simulations, and for three layers of the atmospheric column, namely the boundary-layer (1000-925 hPa), the lower free troposphere (850-700 hPa) and the mid free troposphere (600-400 hPa). The layers are chosen according to the tendency vertical profiles, but the following results weakly depends on the exact pressure levels chosen to define these layers.

After the first phase of self-aggregation in the 305-K simulation, all tendencies in the dry regions remain approximately constant, except within the boundary layer (Figure 14). As convection continues to self-aggregate, the boundary-layer heating by turbulent processes increases and is slightly enhanced by the weakly increasing cloudy-sky LW radiative heating, and weakened by the increasing cooling by convective and large-scale microphysical processes (i.e. condensation and evaporation). The total effect of diabatic processes is balanced by a weak, slightly increasing, advective cooling. The boundary-layer potential temperature budget thus depicts an increased mixing within the boundary layer, most probably due to both an increased of the buoyancy surface flux and the free troposphere air entrainment at the boundary-layer top, together with more low-level cloudiness at its top (see also Figure 11) and enhanced evaporation of weakly-precipitating cumulus or stratocumulus.

In contrast, in the boundary layer of the wet regions (Figure 15k-o), the turbulent and cloudy-sky LW radiative heating rates weakly evolve after the first self-aggregation phase, while the heating by convective and large-scale condensation significantly increases. It is slightly reinforced by the reducing clear-sky LW radiative cooling. Above, the potential temperature budget is mainly controlled by the convection and large-scale microphysical heating, which is consistent with diabatic heating profiles becoming more bottom-heavy. This is counterbalanced by the advective cooling. Thus, the boundary-layer temperature contrast evolution, thereby generating geopotential horizontal gradients which can enhance the shallow circulation (Figure 6b,g,m), mostly rely on turbulent processes within dry regions and convection or large-scale condensation within moist regions. Above, in the lower and mid free troposphere, the increasing condensational heating in moist regions also favors the strengthening of the shallow circulation upper branch.

Nevertheless, after the first self-aggregation phase, most potential temperature tendencies approximately follow the same trajectory across the four SSTs displayed on Figures 14 and 15, with only a few exceptions. The clear-sky LW radiative tendency within dry regions exhibits a clear sensitivity to SST at the end of the first self-aggregated state. In the free troposphere, the advective tendency mostly mirrors this clear-sky LW radiative tendency, consistently with a large-scale subsidence mostly driven by radiative processes. In the boundary layer, turbulent mixing processes partially compensate the destabilization of the lower part of the column by clear-sky LW radiative cooling.

As a result, the following picture of the second self-aggregation phase is suggested. After the first phase of self-aggregation, higher SSTs drives higher LW radiative cooling in the dry regions, both within the boundary layer and mid free troposphere (around 600-400 hPa). In the boundary layer, though the destabilization increased by radiative processes is partially balanced by an enhanced turbulent mixing, the temperature contrast with moist regions enhances the dry-to-moist region pressure gradient and thus the lower branch of the shallow and deep circulations. Above, the enhanced radiative cooling strengthens the large-scale subsidence, drying further the free troposphere and thereby providing a drier environment for convective updrafts. Their dilution is enhanced at upper levels, which thus leads to more bottom-heavy diabatic heating profiles. This further enhances the shallow circulation, driving a positive feedback on deep convection. As convective/moist regions become less mobile, radiative feedbacks can reinforce their local effect, i.e. enhancing the drying effect of the radiatively-driven large-scale subsidence and enhancing the boundary-layer pressure gradient between dry and moist regions. This occurs until a new equilibrium is achieved. Cloud processes further feeds back positively during this second phase of self-aggregation.

5 Conclusions and discussions

In this study, we investigate convective self-aggregation in the CNRM-CM6-1 general circulation model and assess its dependence to sea surface temperature (SST) in the non-rotating radiative-convective equilibrium (RCE) framework as defined within the RCEMIP exercise (Wing et al., 2018). We use the three simulations run for this project (homogeneous SST of 295, 300 and 305 K), supplemented by 5-member ensembles at the RCEMIP SSTs and additional experiments exploring intermediate SSTs between 295 K and 305 K. In all numerical experiments, self-aggregation occurs within the first 20 days, at a slightly faster pace at lower SST. As SST increases, the self-aggregated equilibrium gets drier, and the large-scale circulation between dry and moist regions exhibits a strengthening shallow component. Low-cloud cover also increases, mostly in the dry regions. As expected from thermodynamical arguments, the top of high clouds rises with increasing SSTs. In contrast to the iris effect found with other models (Bony et al., 2016), high-cloud fraction does not exhibit any clear monotonic shrinking tendency with increasing SSTs, except below 298 K. High-cloud fraction does diminish in dry region, but high clouds become thicker or more frequent in moist convectively-active regions. This behavior may be consistent with the high equilibrium sensitivity in the CNRM-CM6-1 and the role of cloudy-sky longwave feedbacks in driving it (Saint-Martin et al., 2021), as a weak or absent iris effect as found here would remove a negative feedback on the climate system.

For all experimented SSTs, CNRM-CM6-1 exhibits a rapid initial phase of self-aggregation similar to that found in other models (e.g., Wing et al., 2017): it primarily involves positive radiative feedbacks, especially in the cloudy-sky longwave and clear-sky shortwave components. At the lowest SSTs, the latent heat flux feedback also favors self-aggregation initiation, but rapidly becomes a strongly negative feedback. Sensible heat fluxes only marginally contribute to self-aggregation at all SSTs, slightly more at colder SSTs. The use of the normalized frozen moist static energy framework of Pope et al. (2021) allows us to more appropriately compare the weights of the various self-aggregation feedbacks at different SSTs. It emphasizes that the clear-sky shortwave and surface enthalpy flux feedbacks are notably weaker at 305 K than at lower SSTs. The stronger feedbacks at low SSTs is thus consistent with a faster initial self-aggregation.

Following this first phase of self-aggregation, simulations with surface temperature above approximately 300 K exhibits a second transition towards a new state of self-aggregation.

This transition is slower, lasting from 150 days at 305 K to more than a year at 300 K. At the beginning of this new transition, a first adjustment of the large-scale geopotential horizontal gradients between moist and dry regions, and thus of the associated circulation, occurs, mostly within the mid-troposphere. Its origin remains so far elusive and requires further work in the future. Then, a progressive shift from a top-heavy circulation to a more bottom-heavy circulation occurs. This clearly does not happen at low SSTs. Thus, at high SSTs, a shallow circulation settles and become even more efficient than its deep counterpart. The degree at which self-aggregation stabilizes seems in particular related to the relative importance between the shallow and the deep circulations (the η metric). The speed of this second phase of self-aggregation also appears connected to that of the shallow circulation efficiency enhancement, similarly to what is found in Shamekh et al. (2020b).

The second phase of self-aggregation occurs simultaneously to several notable changes. As mentioned above, a shallow circulation settles and becomes stronger than the deep circulation. Convective moist regions become less mobile. Dry regions get significantly drier and occupy wider areas, while moist regions only marginally get moister. Positive advection feedbacks appears in the driest regions. The occurrence of this second phase seems primarily driven by clear-sky radiative processes in dry regions, both within the boundary layer and the mid free troposphere. As discussed in Naumann et al. (2017, 2019) and Shamekh et al. (2020a) and Yang (2018), the enhanced differential radiative cooling in the boundary layer at higher SSTs increases the pressure gradient between dry and moist regions, which thus strengthens the lower branch of the shallow and deep circulations. Above, in the dry regions neighboring moist regions, the enhanced radiative cooling enhances the large-scale subsidence, drying further the free troposphere, and thereby providing a drier environment for convective updrafts. Their dilution is likely enhanced at mid and upper levels, thereby leading to more bottom-heavy diabatic heating profiles. This further enhances the shallow circulation, which positively feed backs on deep convection. Besides, the fact that convection is less mobile allows the strengthening of all previous mechanisms, as they can act on the same place for a longer period of time. Cloud processes also act as another positive feedback during this transition. This schematic remains an hypothesis, albeit consistent with the diagnostics provided in this manuscript. It will be further tested in the future through dedicated experiments.

In addition to more classical metrics of self-aggregation, we propose in this work a more detailed framework to characterize the CRH spatial distribution and its temporal evolution: the CRH distribution, when bi-modal, can be well approximated by two log-normal distributions describing the properties of the dry and moist regions. The associated diagnostics emphasize that transition to self-aggregation and self-aggregated states in CNRM-CM6-1 is mostly driven by adjustments within the dry regions, both in terms of level of dryness and of covered area. Applying these diagnostics to the RCEMIP ensemble might help better link self-aggregation levels and the CRH distribution and understand why self-aggregation usually increases with SST in GCMs but not necessarily in CPMs.

Finally, the long timescale of self-aggregation in CNRM-CM6-1 (150 to 400 days depending on SSTs) questions the way GCM and CPM RCE simulations are compared, as within the RCEMIP framework. GCMs are run over about 3 years while CPM simulations only last 100 days. The latter may not be enough to achieve equilibrium and may explain some of the strong differences between GCM and CPM RCE states and their sensitivity to SSTs. This calls for further investigation in the future, to assess whether CNRM-CM6-1 has a peculiar, unusual behavior or CPMs do further self-aggregate on longer timescales.

Appendix A

In this paper, the large-scale circulation is characterized through the streamfunction within a rank of CRH–pressure plan. To compute the streamfunction Ψ, the 32768 columns are ordered from the lowest to the highest CRH and averaged by groups of 32 columns. The 1016 groups of columns are given an index $i = 1, 2, \ldots, 1024$. Then, Ψ is calculated as a horizontal integral of the vertical velocity averaged over each of these groups, starting from the driest column ($i = 1$):

$$\Psi_i(z) = \Psi_{i-1}(z) + w_i(z)\overline{\rho}(z) \quad \text{(A1)}$$

with $\Psi_{i=0}(z) = 0$ for all z, w the vertical velocity and $\overline{\rho}$ the mean density profile. Thus, Ψ_i(z) can be interpreted as the net upward mass flux at height z accumulated over the i driest blocks.

The vertical structure of the streamfunction shows two cells: a shallow circulation with a maximum below 750 hPa and a deeper cell with a maximum above 500 hPa. To calculate the contribution of the shallow circulation to the total circulation (shallow + deep), Shamekh et al. (2020b) define the circulation efficiency η as:

$$\eta = \frac{\Psi_{\max} - \Psi_{\min}}{\Psi_{\max,\text{deep}} + \Psi_{\max} - \Psi_{\min}} \tag{A2}$$

with $\Psi_{\max}$, the maximum of the shallow circulation, $\Psi_{\max,\text{deep}}$, the maximum of the deep circulation and $\Psi_{\min}$, the local streamfunction minimum between them.

The numerator is the net boundary-layer mass divergence out of dry regions into moist regions, which returns to the dry regions below the height of the minimum, around 600 hPa. The denominator quantifies the overall large-scale circulation strength, measured by the total mass transport from dry to moist regions. Thus η (between 0 and 1) measures the fraction of mass transport from dry to moist regions performed by the shallow circulation.

Appendix B

To quantify how much moist/convectively-active regions are mobile, we calculate the correlation between the CRH map of a given day and that of each of the following days (noted ρ_{CRH}). We then identify the lead time (in days) when the correlation goes below 0.5 (noted d(ρ_{CRH}=0.5)). This quantifies how long the CRH map remains approximately similar. Results remains qualitatively similar when using precipitable water or correlation thresholds of 0.3 and 0.8.

Open Research

Hourly output of the 295-K, 300-K and 305-K RCEMIP CNRM-CM6-1 simulations are part of the RCEMIP dataset, publicly available at `http://hdl.handle.net/21.14101/d4beee8e-6996-453e-bbd1-ff53b6874c0e`. Daily output for the 295–305-K RCEMIP-style simulations and for each member of the 295-K, 300-K and 305-K ensembles, used in the present paper, are publicly available at `https://thredds-su.ipsl.fr/thredds/catalog/rcemip/catalog.html`. A permanent identifier will be created if the present paper is accepted. Hourly output for the 302-K RCEMIP-style simulation, the ARPEGE-Climat software (Version 6.3) used for running the simulations, and the scripts used in the analysis are available upon request to the corresponding author.

Acknowledgments

This project has received funding from the European Union's Horizon 2020 research and innovation programme under grant agreement No 820829. We thanks the German Climate Computing Center (DKRZ) for hosting the standardized RCEMIP data.

References

Becker, T., & Stevens, B. (2014). Climate and climate sensitivity to changing CO2 on an idealized land planet. *Journal of Advances in Modeling Earth Systems*, *6*, 513–526. doi: 10.1002/2014MS000369

Becker, T., Stevens, B., & Hohenegger, C. (2017). Imprint of the convective parameterization and sea-surface temperature on large-scale convective self-aggregation. *Journal of Advances in Modeling Earth Systems*, *9*. doi: 10.1002/2016MS000865

Becker, T., & Wing, A. A. (2020). Understanding the Extreme Spread in Climate Sensitivity within the Radiative-Convective Equilibrium Model Intercomparison Project. *Journal of Advances in Modeling Earth Systems*, *12*(10). doi: 10.1029/2020MS002165

Bellenger, H., Duvel, J. P., Lengaigne, M., & Levan, P. (2009). Impact of organized intraseasonal convective perturbations on the tropical circulation. *Geophysical Research Letters*, *36*(16), 1–5. doi: 10.1029/2009GL039584

Bony, S., Stevens, B., Coppin, D., Becker, T., Reed, K. A., Voigt, A., & Medeiros, B. (2016). Thermodynamic control of anvil cloud amount. *Proceedings of the National Academy of Sciences of the United States of America*, *113*(32), 8927–8932. doi: 10.1073/pnas.1601472113

Bougeault, P., & Lacarrere, P. (1989). Parameterization of orography-induced turbulence in a mesobeta–scale model. *Monthly weather review*, *117*(8), 1872–1890. doi: 10.1175/1520-0493(1989)117⟨1872:POOITI⟩2.0.CO;2

Bretherton, C. S., Blossey, P. N., & Khairoutdinov, M. (2005). An energy-balance analysis of deep convective self-aggregation above uniform SST. *Journal of the Atmospheric Sciences*, *62*(12), 4273–4292. doi: 10.1175/JAS3614.1

Bretherton, C. S., McCaa, J. R., & Grenier, H. (2004). A new parameterization for shallow cumulus convection and its application to marine subtropical cloud-topped boundary layers. Part I: Description and 1D results. *Monthly*

Weather Review, *132*(4), 864–882. doi: 10.1175/1520-0493(2004)132⟨0864:ANPFSC⟩2.0.CO;2

Coppin, D., & Bellon, G. (2019a). Physical Mechanisms Controlling the Offshore Propagation of Convection in the Tropics: 1. Flat Island. *Journal of Advances in Modeling Earth Systems*, *11*(9), 3042–3056. doi: 10.1029/2019MS001793

Coppin, D., & Bellon, G. (2019b). Physical Mechanisms Controlling the Offshore Propagation of Convection in the Tropics: 2. Influence of Topography. *Journal of Advances in Modeling Earth Systems*, *11*(10), 3251–3264. doi: 10.1029/2019MS001794

Coppin, D., & Bony, S. (2015). Physical mechanisms controlling the initiation of convective self-aggregation in a General Circulation Model. *Journal of Advances in Modeling Earth Systems*, *7*, 2060–2078. doi: 10.1002/2015MS000571

Coppin, D., & Bony, S. (2017). Internal variability in a coupled general circulation model in radiative-convective equilibrium. *Geophysical Research Letters*, *44*(10), 5142–5149. doi: 10.1002/2017GL073658

Coppin, D., & Bony, S. (2018). On the Interplay Between Convective Aggregation, Surface Temperature Gradients, and Climate Sensitivity. *Journal of Advances in Modeling Earth Systems*, *10*(12), 3123–3138. doi: 10.1029/2018MS001406

Craig, G. C., & Mack, J. M. (2013). A coarsening model for self-organization of tropical convection. *Journal of Geophysical Research Atmospheres*, *118*(16), 8761–8769. doi: 10.1002/jgrd.50674

Cronin, T. W., & Wing, A. A. (2017). Clouds, Circulation, and Climate Sensitivity in a Radiative-Convective Equilibrium Channel Model. *Journal of Advances in Modeling Earth Systems*, *9*(8), 2883–2905. doi: 10.1002/2017MS001111

Cuxart, J., Bougeault, P., & Redelsperger, J. L. (2000). A turbulent scheme allowing for mesoscale and large-eddy simulations. *Quarterly Journal of the Royal Meteorological Society*, *130*(604), 3055–3079. doi: 10.1256/qj.03.130

Fouquart, Y., & Bonnel, B. (1980). Computations of solar heating of the Earth's atmosphere—A new parameterization. *Beiträge zur Phys der Atmosphäre*, *53*, 35–62.

Gueremy, J. F. (2011). A continuous buoyancy based convection scheme: One- and three-dimensional validation. *Tellus, Series A: Dynamic Meteorology and*

Oceanography, *63*(4), 687–706. doi: 10.1111/j.1600-0870.2011.00521.x

Hartmann, D. L., & Larson, K. (2002). An important constraint on tropical cloud - climate feedback. *Geophysical Research Letters*, *29*(20), 12-1-12-4. doi: https://doi.org/10.1029/2002GL015835

Hohenegger, C., & Stevens, B. (2018). The role of the permanent wilting point in controlling the spatial distribution of precipitation. *Proceedings of the National Academy of Sciences of the United States of America*, *115*(22), 5692–5697. doi: 10.1073/pnas.1718842115

Holloway, C. E., Wing, A. A., Bony, S., Muller, C., Masunaga, H., L'Ecuyer, T. S., ... Zuidema, P. (2017). Observing Convective Aggregation. *Surveys in Geophysics*, *38*(6), 1199–1236. doi: 10.1007/s10712-017-9419-1

Holloway, C. E., & Woolnough, S. J. (2016). The sensitivity of convective aggregation to diabatic processes in idealized radiative-convective equilibrium simulations. *Journal of Advances in Modeling Earth Systems*, *8*, 166–195. doi: 10.1002/2016MS000625

Hortal, M., & Simmons, A. J. (1991). Used of Reduced Gaussian Grids in Spectral Models. *Monthly Weather Review*, *119*, 1057–1074. doi: 10.1175/1520-0493(1991)119⟨1057:UORGGI⟩2.0.CO;2

Houze, R. A. (2004). Mesoscale convective systems. *Reviews of GeophysicsGeophysics*, *104*, 237–286. doi: 10.1016/B978-0-12-374266-7.00009-3

Khairoutdinov, M., & Emanuel, K. (2013). Rotating radiative-convective equilibrium simulated by a cloud-resolving model. *Journal of Advances in Modeling Earth Systems*, *5*(4), 816–825. doi: 10.1002/2013MS000253

Kiladis, G. N., Wheeler, M. C., Haertel, P. T., Straub, K. H., & Roundy, P. E. (2009). Convectively coupled equatorial waves. *Reviews of Geophysics*, *47*(2), 1–42. doi: 10.1029/2008RG000266

Lopez, P. (2002). Implementation and validation of a new prognostic large-scale cloud and precipitation scheme for climate and data-assimilation purposes. *Quarterly Journal of the Royal Meteorological Society*, *128*(579), 229–257. doi: 10.1256/00359000260498879

Madden, R. A., & Julian, P. R. (1994). Observations of the 40-50-day tropical oscillation - a review. *Monthly Weather Review*, *122*(5), 814–837. doi: 10.1175/1520-0493(1994)122⟨0814:OOTDTO⟩2.0.CO;2

Mlawer, E. J., Taubman, S. J., Brown, P. D., Iacono, M. J., & Clough, S. A. (1997). Radiative transfer for inhomogeneous atmospheres: RRTM, a validated correlated-k model for the longwave. *Journal of Geophysical Research Atmospheres*, *102*(14), 16663–16682. doi: 10.1029/97jd00237

Morcrette, J.-J., Barker, H. W., Cole, J. N. S., Iacono, M. J., & Pincus, R. (2008). Impact of a New Radiation Package, McRad, in the ECMWF Integrated Forecasting System. *Monthly Weather Review*, *136*(12), 4773–4798. doi: 10.1175/2008MWR2363.1

Muller, C. J., & Bony, S. (2015). What favors convective aggregation and why? *Geophysical Research Letters*, *42*(13), 5626–5634. doi: 10.1002/2015GL064260

Muller, C. J., & Held, I. M. (2012). Detailed investigation of the self-aggregation of convection in cloud-resolving simulations. *Journal of the Atmospheric Sciences*, *69*(8), 2551–2565. doi: 10.1175/JAS-D-11-0257.1

Naumann, A. K., Stevens, B., & Hohenegger, C. (2019). A moist conceptual model for the boundary layer structure and radiatively driven shallow circulations in the trades. *Journal of the Atmospheric Sciences*, *76*(5), 1289–1306. doi: 10.1175/JAS-D-18-0226.1

Naumann, A. K., Stevens, B., Hohenegger, C., & Mellado, J. P. (2017). A conceptual model of a shallow circulation induced by prescribed low-level radiative cooling. *Journal of the Atmospheric Sciences*, *74*(10), 3129–3144. doi: 10.1175/JAS-D-17-0030.1

Piriou, J. M., Guérémy, J. F., & Bouteloup, Y. (2018). *A subgrid convection scheme for representing dry, moist and precipitating convection in large-scale models, PCMT. Part 1: equations* (Tech. Rep. No. 32). Toulouse, France: CNRM. Retrieved from `http://www.umr-cnrm.fr/IMG/pdf/gueremy_part1_note-cnrm_f.pdf`

Piriou, J. M., Redelsperger, J. L., Geleyn, J. F., Lafore, J. P., & Guichard, F. (2007). An approach for convective parameterization with memory: Separating microphysics and transport in grid-scale equations. *Journal of the Atmospheric Sciences*, *64*(11), 4127–4139. doi: 10.1175/2007JAS2144.1

Pope, K. N., Holloway, C. E., Jones, T. R., & Stein, T. H. M. (2021). Cloud-radiation interactions and their contributions to convective self-aggregation.

Journal of Advances in Modeling Earth Systems, *13*(9), e2021MS002535. doi: 10.1029/2021MS002535

Popke, D., Stevens, B., & Voigt, A. (2013). Climate and climate change in a radiative-convective equilibrium version of ECHAM6. *Journal of Advances in Modeling Earth Systems*, *5*(1), 1–14. doi: 10.1029/2012MS000191

Raymond, D. J., Sessions, S. L., Sobel, A. H., & Fuchs, Ž. (2009). The Mechanics of Gross Moist Stability. *Journal of Advances in Modeling Earth Systems*, *1*(3). doi: 10.3894/JAMES.2009.1.9

Roehrig, R., Beau, I., Saint-Martin, D., Alias, A., Decharme, B., Guérémy, J. F., ... Sénési, S. (2020). The CNRM Global Atmosphere Model ARPEGE-Climat 6.3: Description and Evaluation. *Journal of Advances in Modeling Earth Systems*, *12*(7), 1–53. doi: 10.1029/2020MS002075

Rotunno, J., Klemp, J. B., & Weisman, M. L. (1988). A theory for Strong, Long-Lived Squall Lines. *Journal of Atmospheric Sciences*, *45*(3), 463–485. doi: 10.1175/1520-0469(1988)045⟨0463:ATFSLL⟩2.0.CO;2

Saint-Martin, D., Geoffroy, O., Voldoire, A., Cattiaux, J., Brient, F., Chauvin, F., ... Valcke, S. (2021). Tracking Changes in Climate Sensitivity in CNRM Climate Models. *Journal of Advances in Modeling Earth Systems*, *13*(6), 1–19. doi: 10.1029/2020MS002190

Shamekh, S., Muller, C., Duvel, J. P., & D'Andrea, F. (2020a). How do ocean warm anomalies favor the aggregation of deep convective clouds? *Journal of the Atmospheric Sciences*, *77*(11), 3733–3745. doi: 10.1175/JAS-D-18-0369.1

Shamekh, S., Muller, C., Duvel, J. P., & D'Andrea, F. (2020b). Self-Aggregation of Convective Clouds With Interactive Sea Surface Temperature. *Journal of Advances in Modeling Earth Systems*, *12*(11). doi: 10.1029/2020MS002164

Stein, T. H., Holloway, C. E., Tobin, I., & Bony, S. (2017). Observed relationships between cloud vertical structure and convective aggregation over tropical ocean. *Journal of Climate*, *30*(6), 2187–2207. doi: 10.1175/JCLI-D-16-0125.1

Tobin, I., Bony, S., Holloway, C. E., Grandpeix, J.-Y., Sèze, G., Coppin, D., ... Roca, R. (2013). Does convective aggregation need to be represented in cumulus parameterizations? *Journal of Advances in Modeling Earth Systems*, *5*(4), 692–703. doi: 10.1002/jame.20047

Tobin, I., Bony, S., & Roca, R. (2012). Observational evidence for relationships between the degree of aggregation of deep convection, water vapor, surface fluxes, and radiation. *Journal of Climate*, *25*(20), 6885–6904. doi: 10.1175/JCLI-D-11-00258.1

Tompkins, A. M., & Craig, G. C. (1998). Radiative-convective equilibrium in a three-dimensional cloud-ensemble model. *Quarterly Journal of the Royal Meteorological Society*, 2073–2097. doi: 10.1002/qj.49712455013

Tompkins, A. M., & Semie, A. G. (2017). Organization of tropical convection in low vertical wind shears: Role of updraft entrainment. *Journal of Advances in Modeling Earth Systems*, *9*, 1046–1068. doi: 10.1002/2016MS000802

Voldoire, A., Saint-Martin, D., Sénési, S., Decharme, B., Alias, A., Chevallier, M., ... Waldman, R. (2019). Evaluation of CMIP6 DECK Experiments With CNRM-CM6-1. *Journal of Advances in Modeling Earth Systems*, *11*(7), 2177–2213. doi: 10.1029/2019MS001683

Wing, A. A. (2019). Self-Aggregation of Deep Convection and its Implications for Climate. *Current Climate Change Reports*, *5*(1), 11–13. doi: 10.1007/s40641-019-00120-3

Wing, A. A., & Cronin, T. W. (2016). Self-aggregation of convection in long channel geometry. *Quarterly Journal of the Royal Meteorological Society*, *142*(694), 1–15. doi: 10.1002/qj.2628

Wing, A. A., Emanuel, K., Holloway, C. E., & Muller, C. (2017). Convective Self-Aggregation in Numerical Simulations: A Review. *Surveys in Geophysics*, *38*(6), 1173–1197. doi: 10.1007/s10712-017-9408-4

Wing, A. A., & Emanuel, K. A. (2014). Physical mechanisms controlling self-aggregation of convection in idealized numerical modeling simulations. *Journal of Advances in Modeling Earth Systemsd*, *6*, 59–74. doi: 10.1002/2013MS000269

Wing, A. A., Reed, K. A., Satoh, M., Stevens, B., Bony, S., & Ohno, T. (2018). Radiative-convective equilibrium model intercomparison project. *Geoscientific Model Development*, *11*(2), 793–813. doi: 10.5194/gmd-11-793-2018

Wing, A. A., Stauffer, C. L., Becker, T., Reed, K. A., Ahn, M. S., Arnold, N. P., ... Zhao, M. (2020). Clouds and Convective Self-Aggregation in a Multimodel Ensemble of Radiative-Convective Equilibrium Simulations. *Journal of Advances in Modeling Earth Systems*, *12*(9), 1–38. doi: 10.1029/2020MS002138

Yang, D. (2018). Boundary Layer Diabatic Processes, the Virtual Effect, and Convective Self-Aggregation. *Journal of Advances in Modeling Earth Systems*, *10*(9), 2163–2176. doi: 10.1029/2017MS001261

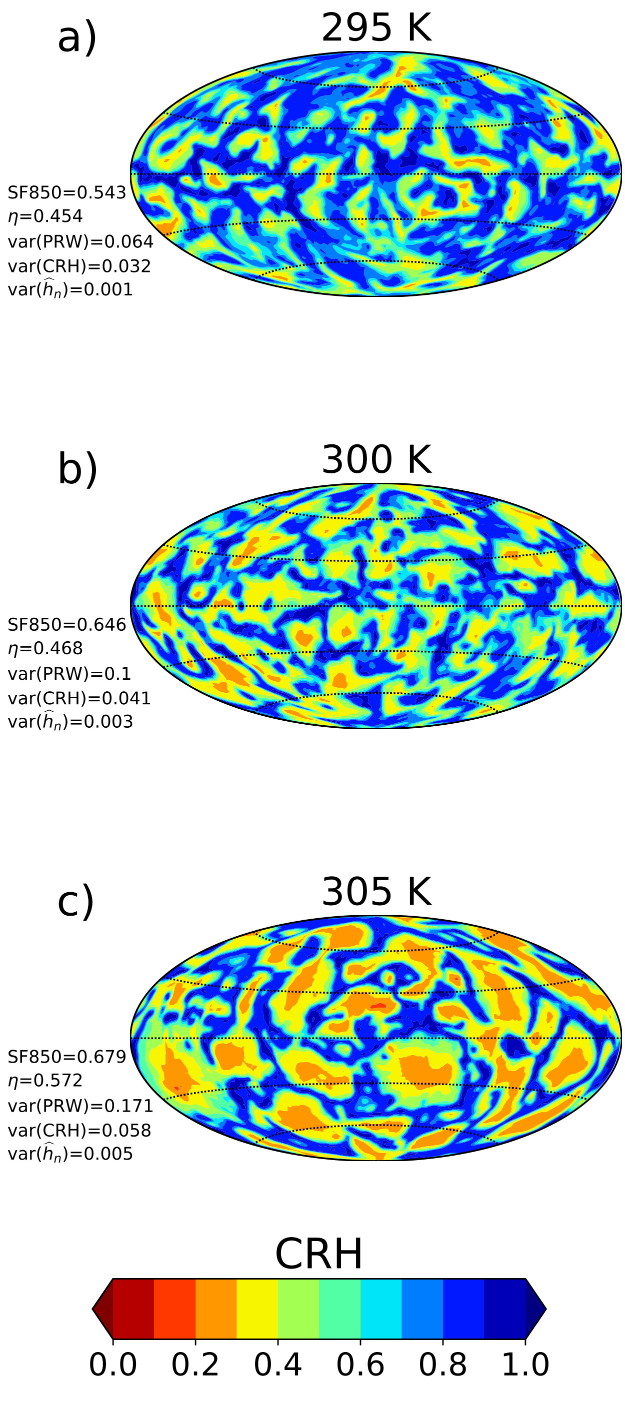

Figure 1. Snapshots of column relative humidity at day 240 of the CNRM-CM6-1 RCE simulations at (a) 295 K, (b) 300 K and (c) 305 K. Different aggregation indices used to characterize convective aggregation are noted in the bottom left corner of each panel (SF850: subsiding fraction considering the pressure vertical velocity at 850 hPa; η: shallow circulation efficiency parameter (see text for detail); var(PRW): spatial variance of precipitable water; var(CRH): spatial variance of CRH; var($\widehat{h}_n$): spatial variance of normalized MSE).

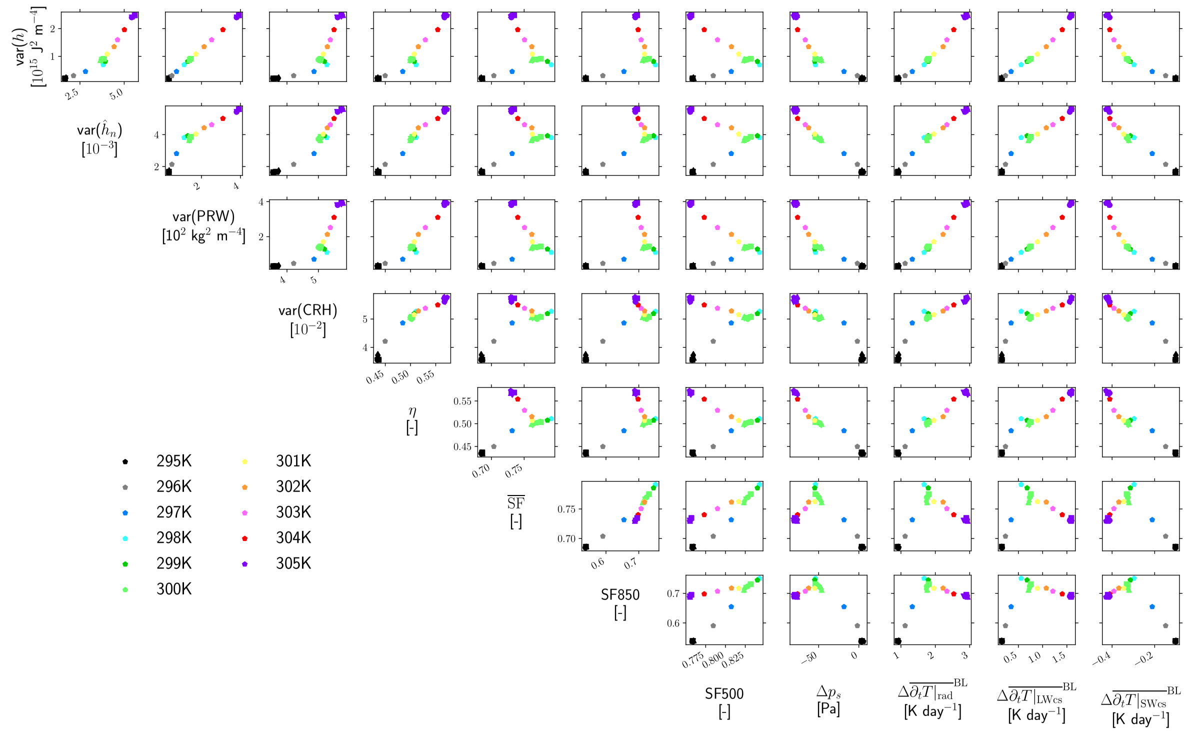

Figure 2. Matrix of the relationships between various indices computed for each SST equilibrium: var($\hat{h}$) (in 10^{15} J^2 m^{-4}), var($\hat{h}_n$) (in 10^{-3}), var(PRW) (in 10^2 kg^2 m^{-4}), var(CRH) (in 10^{-2}), η, $\overline{\text{SF}}$, SF850 and SF500 (see text for their definition). Each panel shows the relationship between two indices as indicated along the matrix diagonal for all SSTs (colors) and for all members of each 295-K, 300-K and 305-K ensemble (same color within each ensemble). The last four columns illustrate the relationships between these indices and the differences between moist and dry regions (Δ symbol) for the surface pressure (Δp_s in Pa) and the boundary-layer net, LW clear-sky and SW clear-sky radiative temperature tendencies ($\Delta\overline{\partial_t T|_{\text{rad}}}^{\text{BL}}$, $\Delta\overline{\partial_t T|_{\text{LWcs}}}^{\text{BL}}$, and $\Delta\overline{\partial_t T|_{\text{SWcs}}}^{\text{BL}}$, respectively, in K day^{-1}). Both regions are defined according to CRH$_c$. The boundary layer values are calculated as the weighted average between 1000 hPa and 925 hPa. Each dot corresponds to the time average over the last year of the corresponding 3-year simulation.

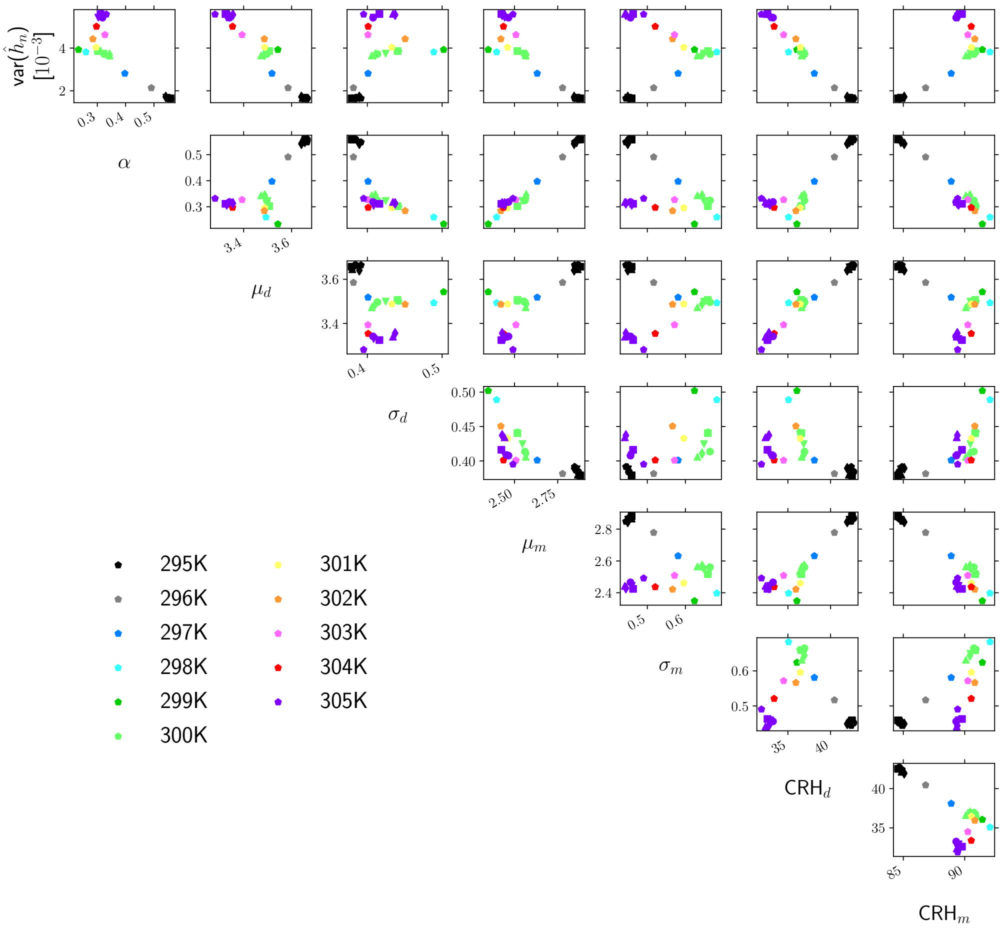

Figure 3. Matrix of the relationships across SSTs between the $\hat{h}_n$ variance (in 10^{-3}) and several parameters describing the CRH distribution at equilibrium: α, μ_d, σ_d, μ_m, σ_m, CRH$_d$ and CRH$_m$ (see Section 2.4 for their definition). Each panel shows the relationship between two indices as indicated along the matrix diagonal for all SSTs (colors) and for all members of each 295-K, 300-K and 305-K ensemble (same color within each ensemble). Each dot corresponds to the time average over the last year of the corresponding 3-year simulation.

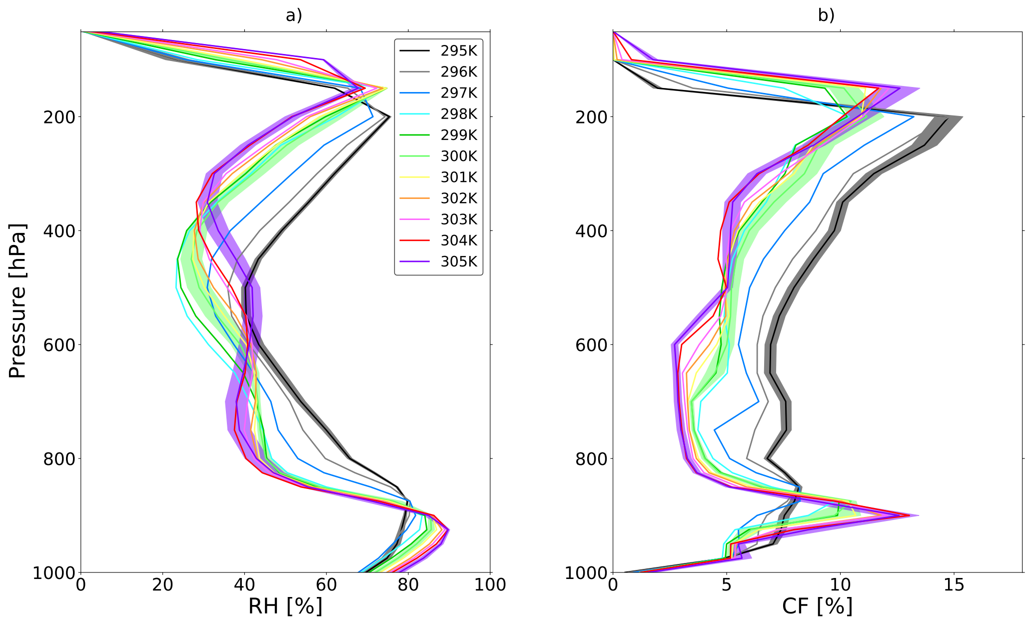

Figure 4. Global mean profile of (a) relative humidity (RH, in %) and (b) cloud fraction (CF, in %) for all SSTs (colored lines). The shading indicates the 3-standard-deviation envelope of the 295-K, 300-K and 305-K ensembles. The time average is performed over the last year of each 3-year simulation.

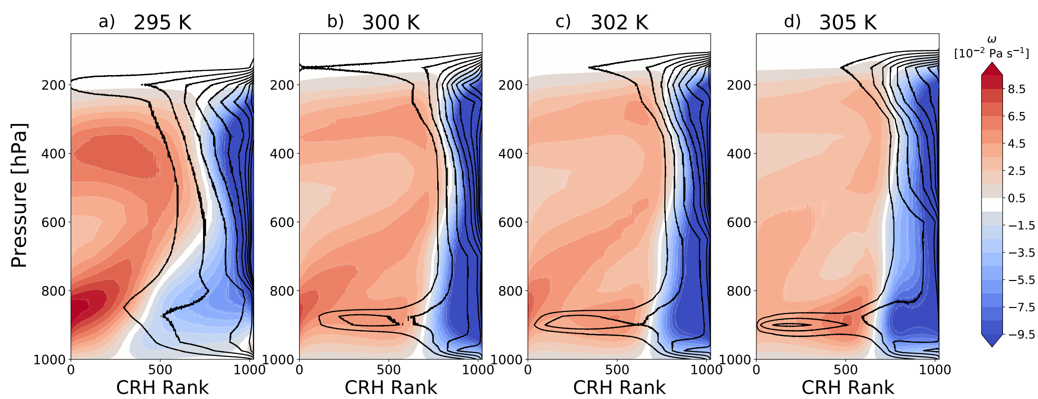

Figure 5. Pressure vertical velocity (colors, in 10^{-2} Pa s^{-1}) and cloud fraction (contours, every 5%) ranked by the daily column relative humidity CRH from dry on the left to moist on the right, for the (a) 295-K, (b) 300-K, (c) 302-K and (d) 305-K simulations. For the sake of clarity, each rank of daily CRH corresponds to the average 32 model columns. Each panel is then an average over the last year of each 3-year simulation.

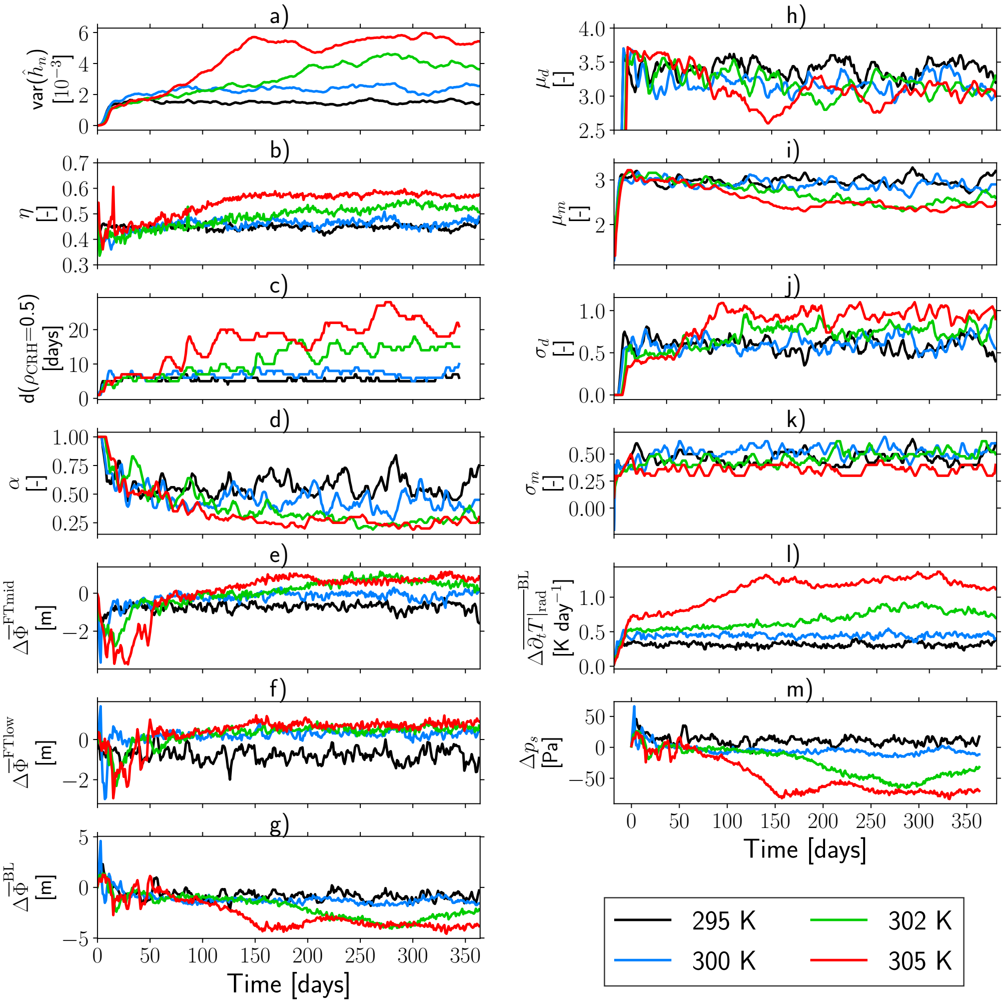

Figure 6. (a) Time evolution of the $\hat{h}_n$ variance over the first year of the 295 K (black), 300 K (blue), 302 K (green) and 305 K (red) simulations. (b-m) Same as (a) but for the shallow circulation efficiency η, the maximum lead time (in days) for which the CRH autocorrelation remains above 0.5 (d(ρ_{CRH}=0.5)), the fraction α of the moist distribution in the CRH full distribution, the geopotential height difference (in m) between moist and dry regions (Δ symbol) integrated over the mid free troposphere (600-400 hPa, $\Delta\overline{\Phi}^{\mathrm{FTmid}}$), the lower free troposphere (850-700 hPa, $\Delta\overline{\Phi}^{\mathrm{FTlow}}$) and the boundary layer (1000-900 hPa, $\Delta\overline{\Phi}^{\mathrm{BL}}$), the CRH distribution parameters (see section 2.4 for details), the radiative temperature tendency difference between moist and dry regions integrated over the boundary layer (1000-900 hPa, $\Delta\overline{\partial_t T|_{\mathrm{rad}}}^{\mathrm{BL}}$ in K day^{-1}) and the surface pressure difference between moist and dry regions (Δp_s in Pa), respectively. Both dry and moist regions are separated according to CRH$_c$.

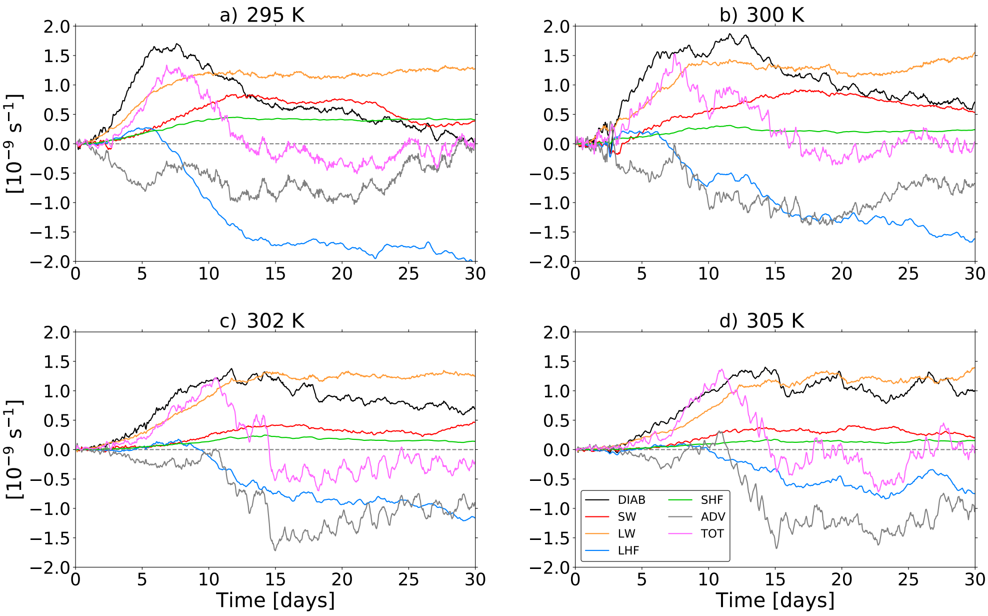

Figure 7. Time evolution of the diabatic (DIAB=SW + LW + LHF + SHF, black), shortwave radiation (SW, red), longwave radiation (LW, orange), latent heat flux (LHF, blue), sensible heat flux (SHF, green), advection (ADV, grey) and total (TOT, purple) feedbacks on the $\hat{h}_n$ variance (in 10^{-9} s^{-1}) for the first 30 days of the (a) 295-K, (b) 300-K, (c) 302-K, and (d) 305-K simulations. The advection feedback is calculated using hourly wind and FMSE model outputs (results are similar when using the more usual residual approach based on Equation 3).

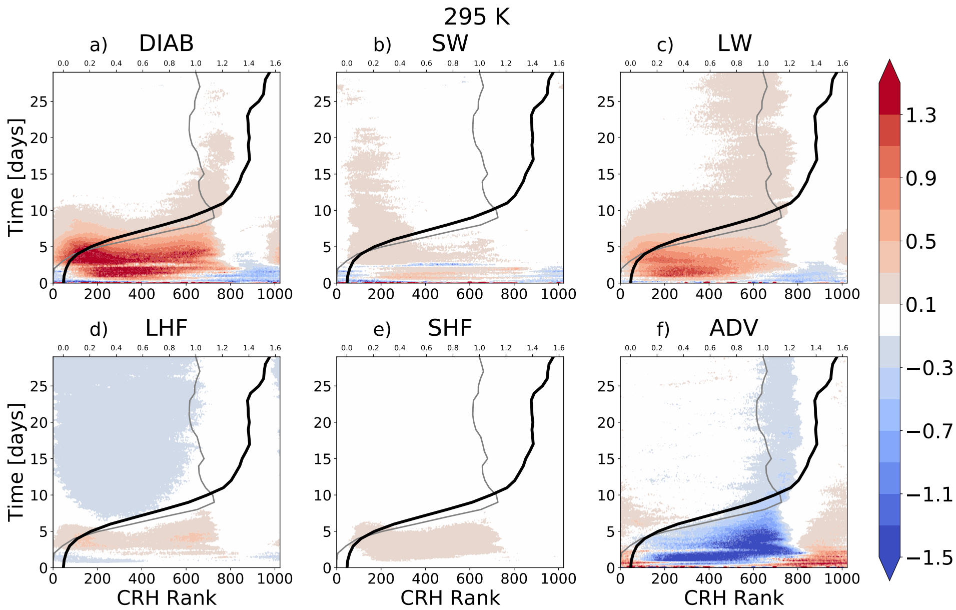

Figure 8. Time evolution of the (a) diabatic (DIAB = SW + LW + LHF + SHF) (b) shortwave radiation (SW), (c) longwave radiation (LW), (d) latent heat flux (LHF), (e) sensible heat flux (SHF), and (f) advection (ADV) feedbacks on the $\hat{h}_n$ variance (in day^{-1}) for the first 30 days of the 295-K simulation and ranked according to the column relative humidity CRH. Feedbacks are normalized at each time step by the corresponding spatial variance of $\hat{h}_n$. The advection feedback is calculated using hourly model outputs. The black and grey solid lines indicate the time evolution of the $\hat{h}_n$ variance (in 10^{-3}, see upper x-axis for its scale) and the CRH rank corresponding to CRH$_c$, respectively.

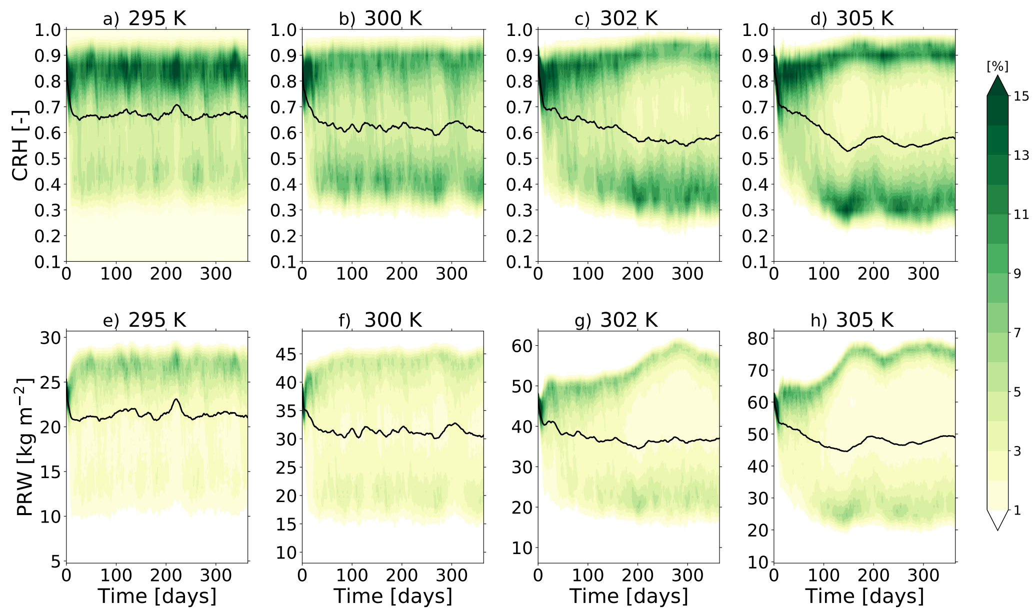

Figure 9. Time evolution of the CRH distribution (in %) for the (a) 295-K, (b) 300-K, (c) 302-K and (d) 305-K simulations. The black line shows the global mean. (e-h) Same as (a-d) for precipitable water.

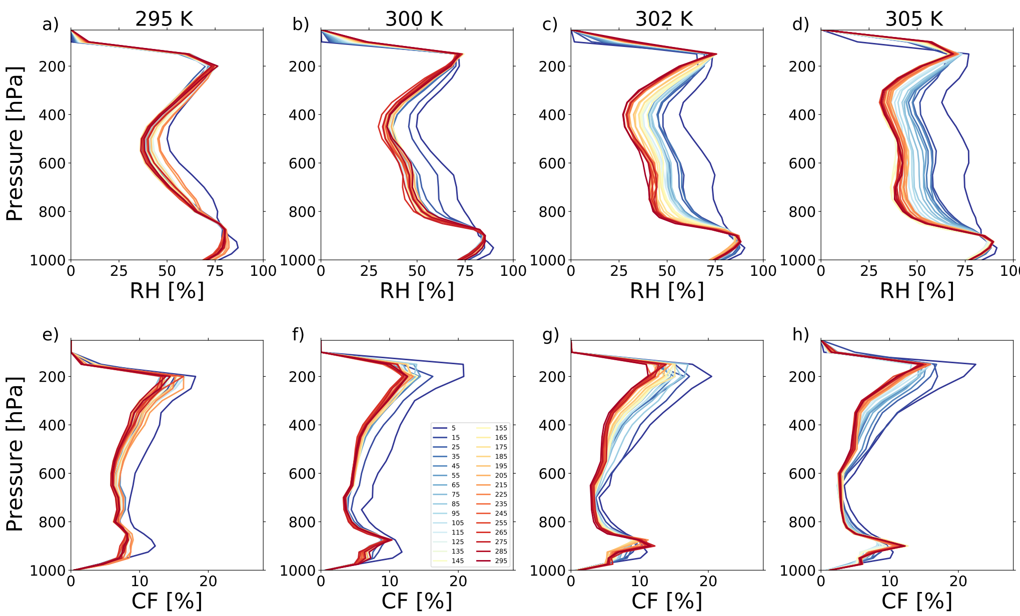

Figure 10. Global mean profile of (a-d) relative humidity (RH, in %) and (e-h) cloud fraction (CF, in %) for the 295-K, 300-K, 302-K and 305-K simulations, respectively. The colors from dark blue to dark red indicate increasing days at which the profile is plotted (from day 5 to day 295, one profile every 5 days).

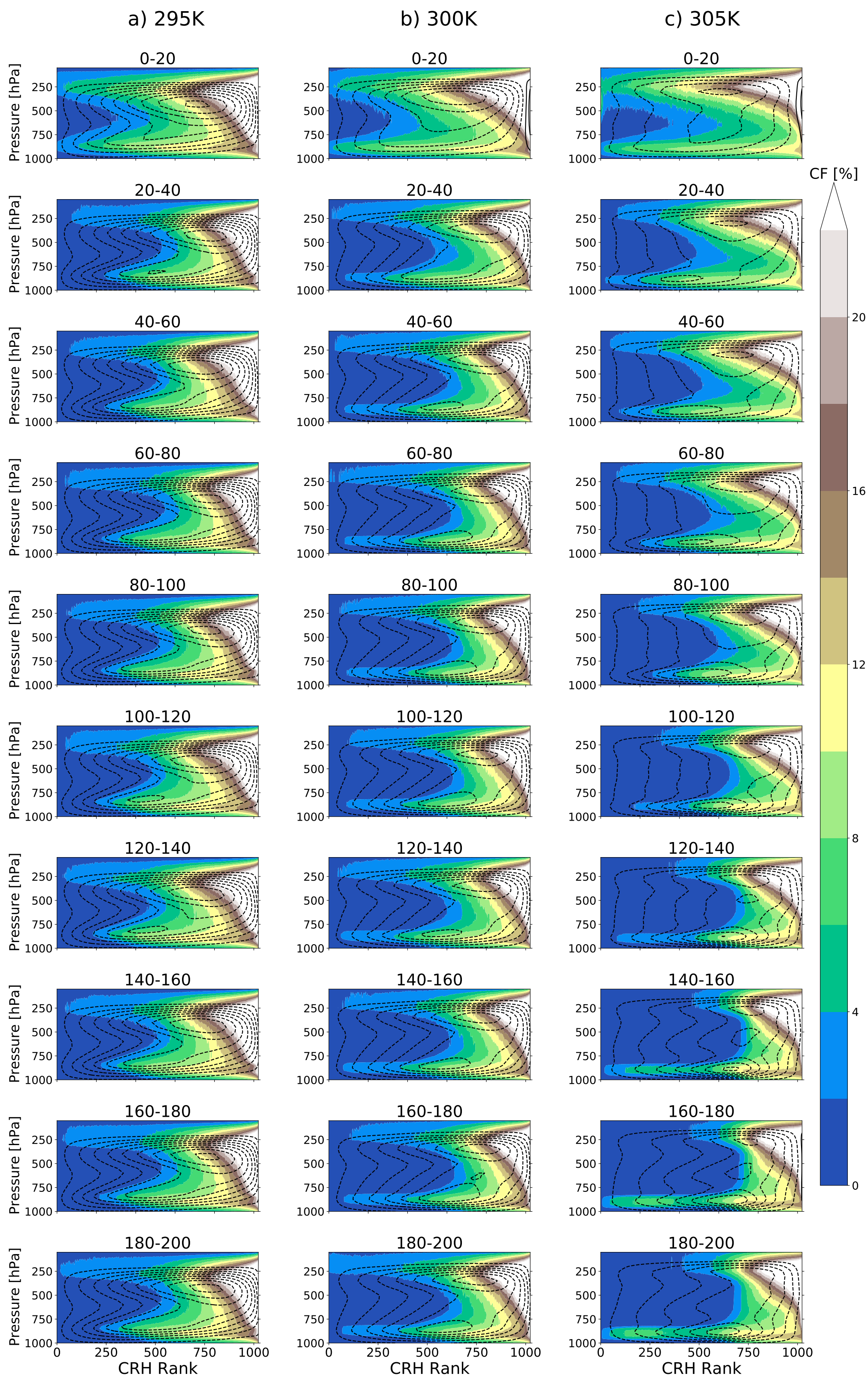

Figure 11. Cloud fraction (colors, in %) and streamfunction (contours, one every 0.5 kg m^{-2} s^{-1}) averaged over 20 consecutive days between days 0 and 200 for the (a) 295-K, (b) 300-K and (c) 305-K simulations. Dashed contours indicate counter-clockwise rotation. For the sake of clarity, each rank of daily CRH corresponds to the average of 32 model columns. Each panel is then the average of 20 diagrams corresponding to the targeted 20 days. The streamfunction is computed from similar average diagrams based on the vertical velocity (see appendix A for details).

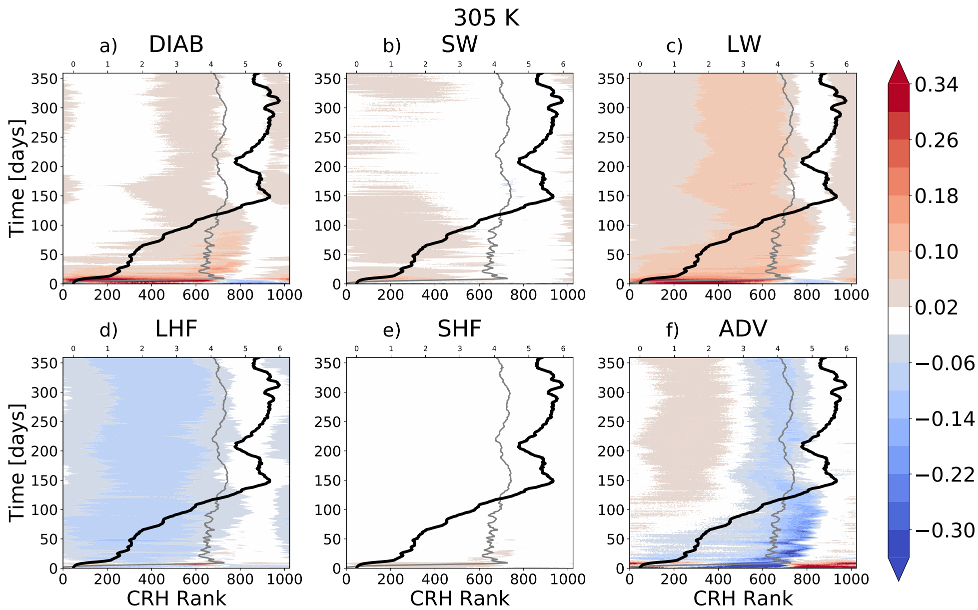

Figure 12. Same as Figure 8 but for the first 360 days of the 305-K simulation.

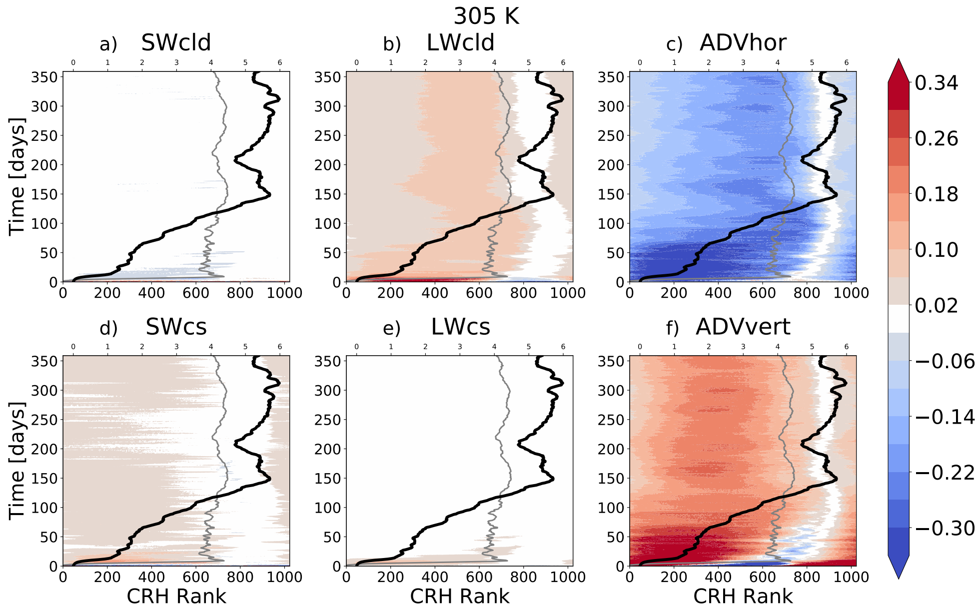

Figure 13. Time evolution of the (a) cloudy-sky shortwave radiation (SWcld), (b) cloudy-sky longwave radiation (LWcld), (c) horizontal advection (ADVhor), (d) clear-sky shortwave radiation (SWcs) (e) clear-sky longwave radiation (LWcs) and (f) vertical advection (ADVvert) feedbacks on the normalized FMSE variance (in day^{-1}) for the first 360 days of the 305-K simulation and ranked according to CRH. Feedbacks are normalized at each time step by the corresponding spatial variance of $\hat{h}_n$. The horizontal and vertical advection feedbacks are calculated using hourly model outputs. The black and grey lines indicate the time evolution of the $\hat{h}_n$ variance (see upper x-axis for its scale) and the CRH rank corresponding to CRH$_c$, respectively.

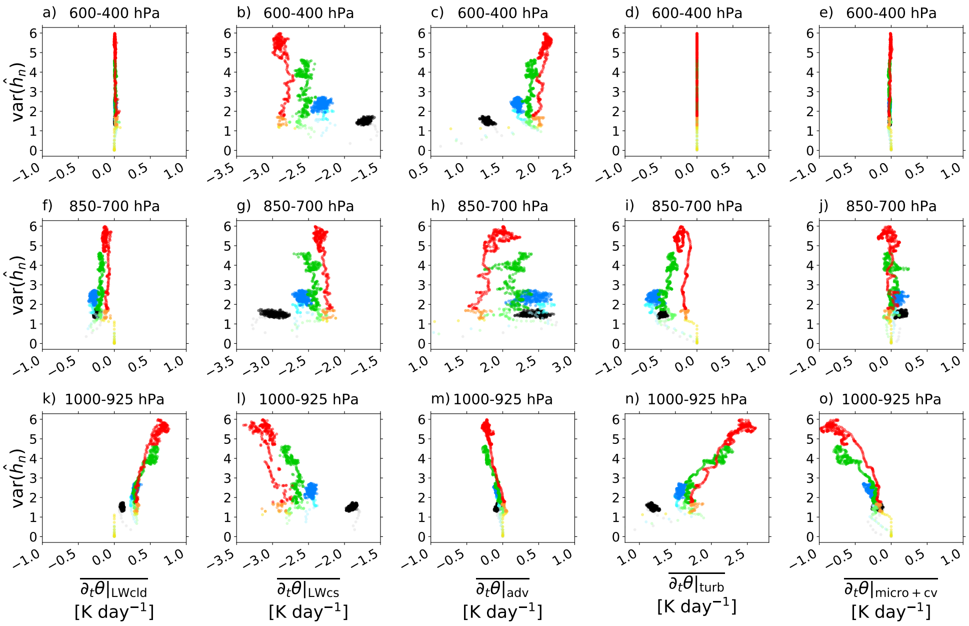

Figure 14. Daily $\hat{h}_n$ spatial variance (in 10^{-3}) evolution over the first year of the 295-K (black), 300-K (blue), 302-K (green) and 305-K (red) simulations as a function of the (a) cloudy-sky longwave radiation, (b) clear-sky longwave radiation, (c) advection, and (d) turbulence potential temperature tendencies ($\overline{\partial_t\theta|_{\mathrm{LWcld}}}$, $\overline{\partial_t\theta|_{\mathrm{LWcs}}}$, $\overline{\partial_t\theta|_{\mathrm{adv}}}$ and $\overline{\partial_t\theta|_{\mathrm{turb}}}$, respectively) and (e) the sum of the convection and large-scale condensation-evaporation ($\overline{\partial_t\theta|_{\mathrm{micro+cv}}}$) temperature tendencies (in K day^{-1}). All terms are averaged over the 600-400-hPa layer and tendencies are daily accumulated. Light colors indicate the first 50 days of each simulation. (f-j) and (k-o) same as (a-e) but for the 850-700-hPa and 1000-925-hPa atmospheric layers, respectively.

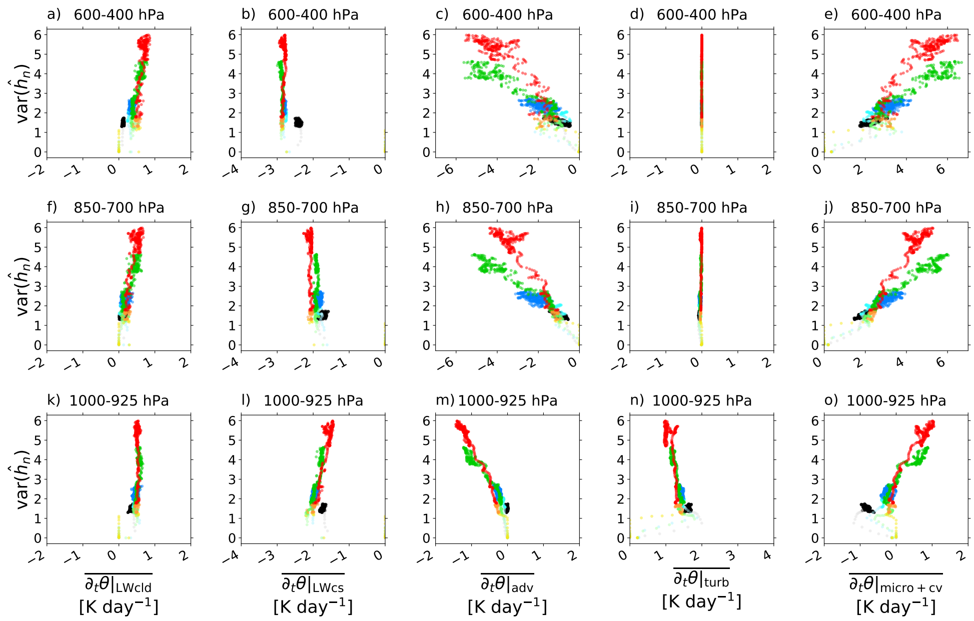

Figure 15. Same as Figure 14 for moist regions.

Supplemental Material for "Convection self-aggregation in CNRM-CM6-1: equilibrium and transition sensitivity to surface temperature"

D. Coppin[1], R. Roehrig[1]

[1]Centre National de Recherches Météorologiques, Université de Toulouse, Météo-France, CNRS, Toulouse, France

Contents of this file

1. Text S1 to S9
2. Figures S1 to S9

Introduction The supplemental material provides additional figures designed to better understand the CRH distribution decomposition into two lognormal distribution and to more comprehensively document the aggregation mechanisms at the SSTs not investigated in details in the main manuscript.

Text S1. Figure S1 illustrates to what extent the sum of a dry and a moist lognormal distribution provides a good approximation of the full CRH distribution for three different time steps of the 305-K simulation.

Text S2. Figure S2 shows how the dry and moist CRH distribution components change with time. In this figure, we see that α, the fraction of the full distribution covered by the moist component, decreases with time as the area below the moist curve becomes smaller than the one below the dry curve. The dry component becomes more peaked with time, which corresponds to a decrease in μ_d. Its skewness also increases towards the dry minimum meaning that σ_d increases with time. For the moist component, σ_m stays mostly constant while μ_m slightly decreases (more peaked distribution). Note that CRH_d and CRH_m, the CRH value at the dry and moist peaks, also change with time: CRH_d decreases and CRH_m increases. The dry and moist components intersect at CRH_c, which is used to distinguish between dry and moist regions.

Texts S3 and S4 Both figures S3 and S4 are similar to Figure 4 and show the relative humidity and cloud fraction profiles in the dry and moist regions separated at each time step by CRH_c, the CRH value where both dry and moist distribution are equal. The mean profile is an average over each day of the last year. It complements Figure 4 in the main manuscript.

Text S5 Figure S5 details the relative contributions of the clear-sky and cloudy-sky radiative feedbacks during the first 30 days of the 295-K, 300-K, 302-K and 305-K simulations. It complements Figure 7 in the main manuscript.

Texts S6 and S7 Figures S6 and S7 are the same as Figure 8 from the main manuscript but for the 300-K and 305-K simulations, respectively.

Text S8 Figure S8 details the clear-sky and cloudy-sky radiative feedbacks at 295 K. It complements Figure 8 in the main manuscript.

Text S9 Figure S9 shows the feedback decomposition for the 302-K simulation. It emphasizes the positive advection feedback that appears in the dry regions as in the simulation at 305 K but later (around day 150 here) while most other feedbacks remain constant after day 20. Equilibrium is reached around day 250. This figure complements Figure 12 in the main manuscript.

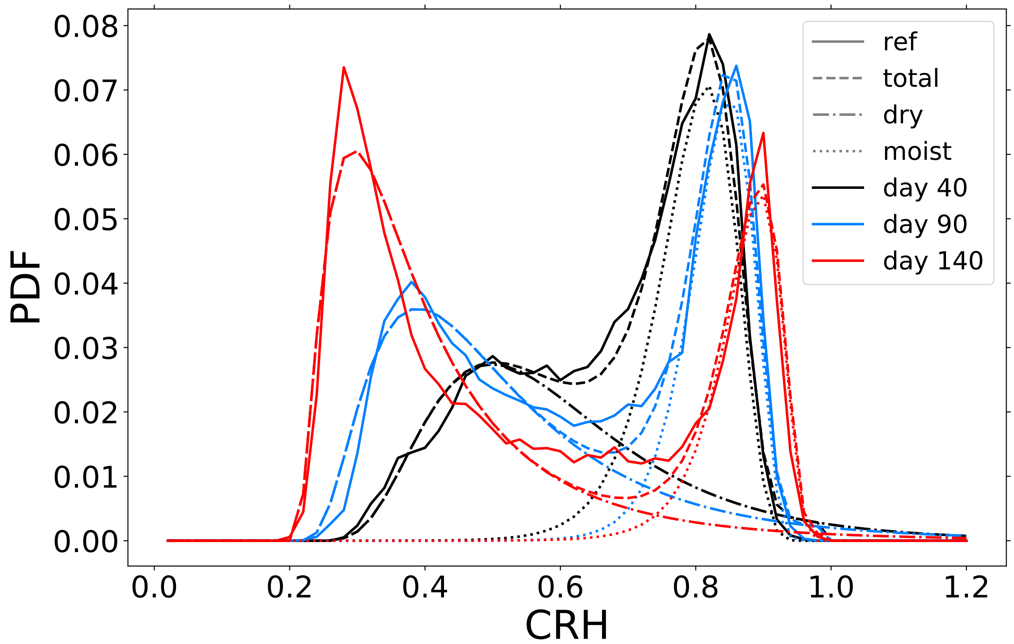

Figure S1. Probability density function of CRH at day 40 (black), day 90 (blue) and day 140 (red) for the 305 K simulation. For each day, the CRH distribution is shown with full line, while its dry and moist lognormal components are shown in dash-dotted and dotted lines, respectively. The sum of the dry and moist lognormal components is shown with dashed lines. See Equation 4 for details.

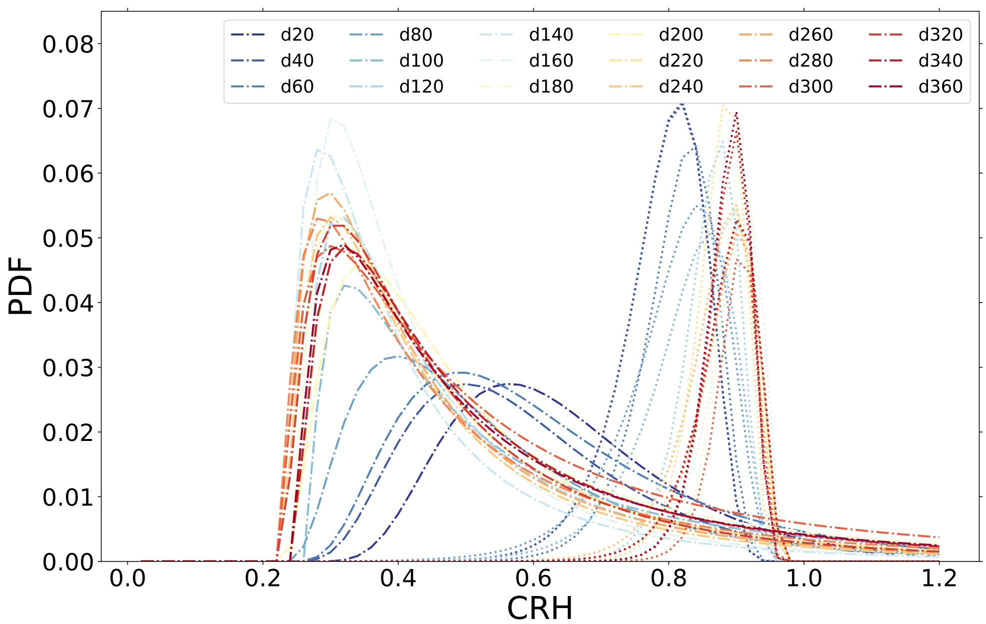

Figure S2. Dry (dash-dotted lines) and moist (dotted lines) components of the CRH probability distribution function estimated by Equation 4 every 20 days of the 305 K simulation. The colors from dark blue to dark red indicate increasing days at which the distributions are plotted.

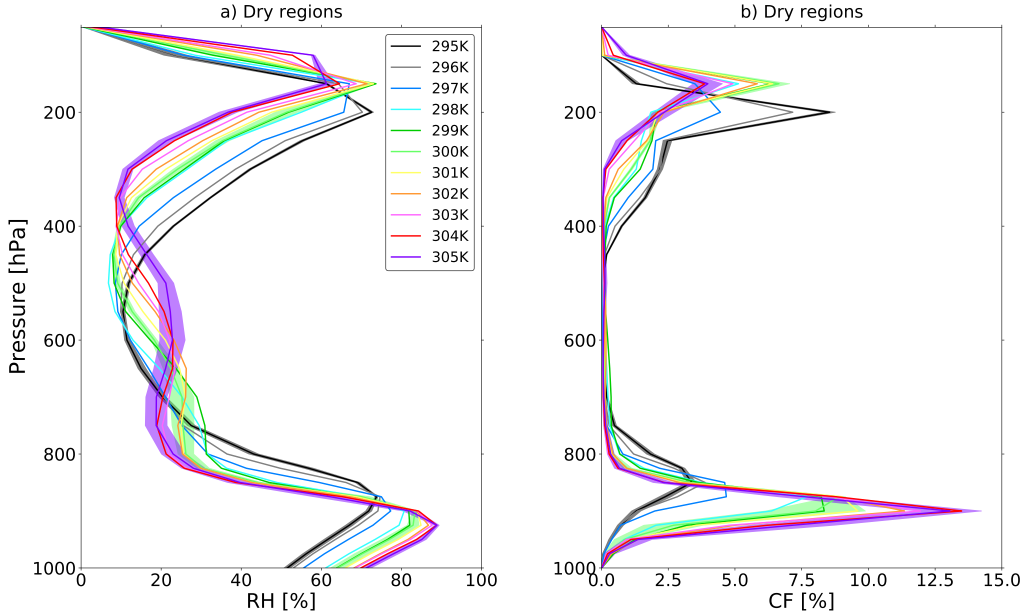

Figure S3. Mean profile of (a) relative humidity (RH, in %) and (b) cloud fraction (CF, in %) in the dry regions of all simulations (colored lines). Dry regions are identified as regions where CRH is lower than CRH_c. The shading indicates the 3-standard-deviation envelope of the 295-K, 300-K and 305-K ensembles. The time average is performed over the last year of each 3-year simulation.

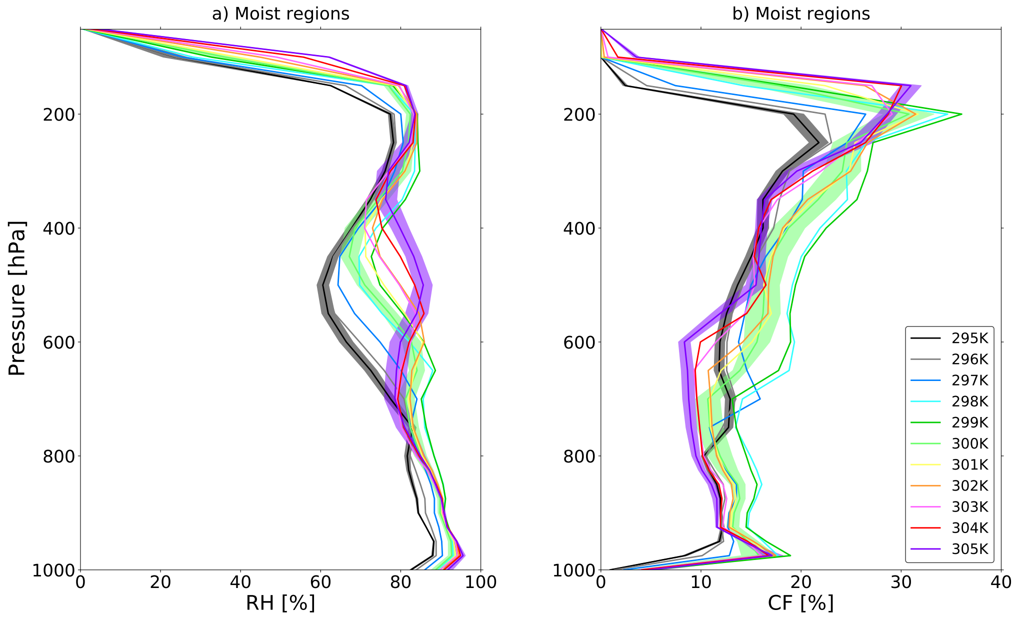

Figure S4. Mean profile of (a) relative humidity (RH, in %) and (b) cloud fraction (CF, in %) in the moist regions of all simulations (colored lines). Moist regions are identified as regions where CRH is higher than CRH_c. The shading indicates the 3-standard-deviation envelope of the 295-K, 300-K and 305-K ensembles. The time average is performed over the last year of each 3-year simulation.

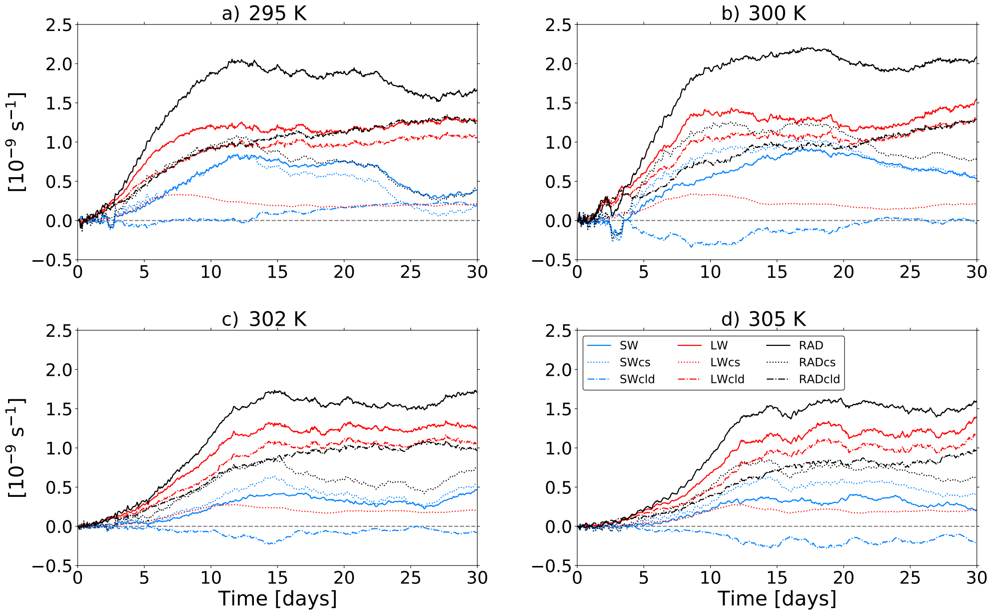

Figure S5. Time evolution of the shortwave (blue), longwave (red) and total (RAD = LW+SW, black) radiation feedbacks on the $\hat{h}_n$ variance (in 10^{-9} s^{-1}) for the first 30 days of the (a) 295-K, (b) 300-K, (c) 302-K and (d) 305-K simulations. For each feedback, the clear-sky, cloudy-sky and total components are indicated with dotted, dash-dotted and solid lines, respectively.

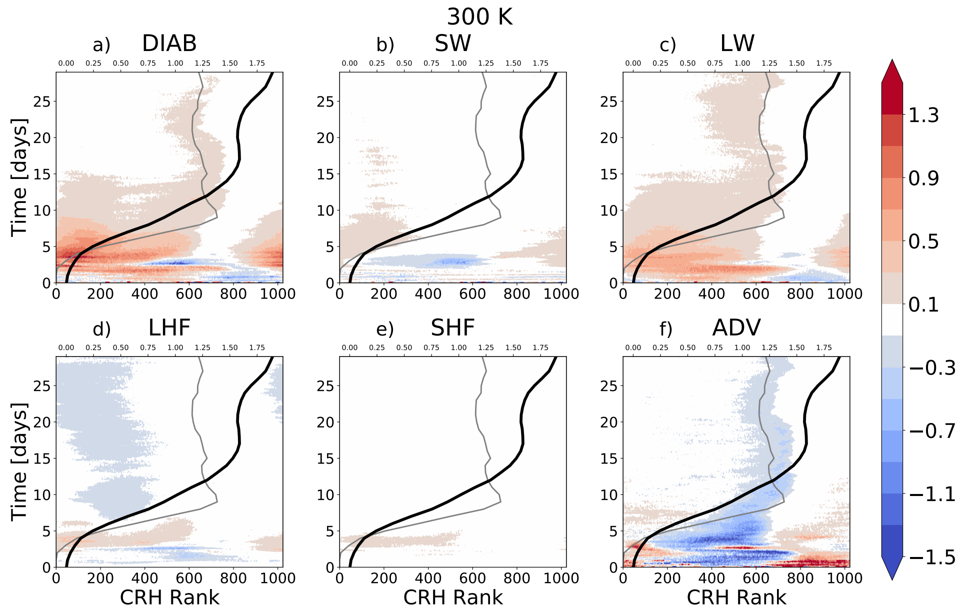

Figure S6. Time evolution of the (a) diabatic (DIAB = SW + LW + LHF + SHF) (b) shortwave (SW), (c) longwave (LW), (d) latent heat flux (LHF), (e) sensible heat flux (SHF), and (f) advection (ADV) feedbacks on the $\hat{h}_n$ variance (in day^{-1}) for the first 30 days of the 300-K simulation and ranked according to the column relative humidity CRH. Feedbacks are normalized at each time step by the corresponding spatial variance of $\hat{h}_n$. The advection feedback is calculated using hourly model outputs. The black and grey solid lines indicate the time evolution of $\hat{h}_n$ variance (in 10^{-3}, see upper x-axis for its scale) and the CRH rank corresponding to CRH$_c$, respectively.

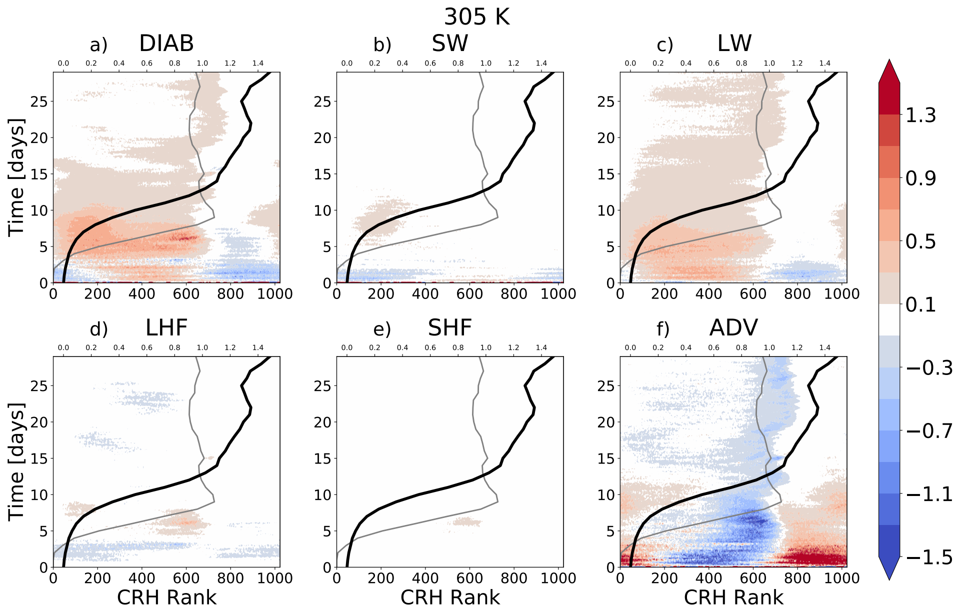

Figure S7. Time evolution of the (a) diabatic (DIAB = SW + LW + LHF + SHF) (b) shortwave radiation (SW), (c) longwave radiation (LW), (d) latent heat flux (LHF), (e) sensible heat flux (SHF), and (f) advection (ADV) feedbacks on the $\hat{h}_n$ variance (in day^{-1}) for the first 30 days of the 305-K simulation and ranked according to the column relative humidity CRH. Feedbacks are normalized at each time step by the corresponding spatial variance of $\hat{h}_n$. The advection feedback is calculated using hourly model outputs. The black and grey solid lines indicate the time evolution of $\hat{h}_n$ variance (in 10^{-3}, see upper x-axis for its scale) and the CRH rank corresponding to CRH$_c$, respectively.

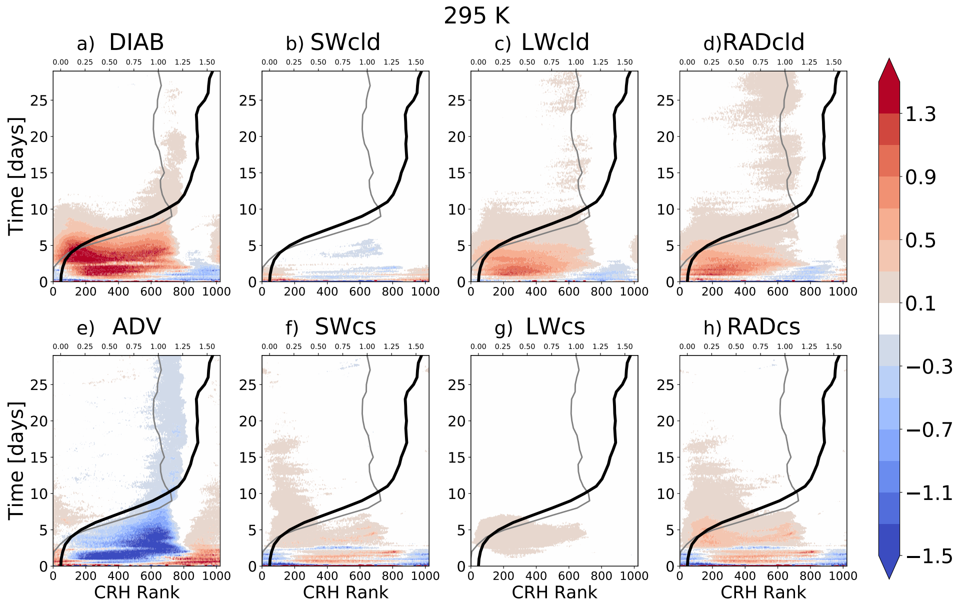

Figure S8. Time evolution of the (a) diabatic (DIAB = SW + LW + LHF + SHF), (b) cloudy-sky shortwave radiation (SWcld), (c) cloudy-sky longwave radiation (LWcld), (d) cloudy-sky radiation (RADcld = LWcld + SWcld), (e) advection (ADV), (f) clear-sky shortwave radiation (SWcs), (g) clear-sky longwave radiation (LWcs) and (h) clear-sky radiation (RADcs = LWcs + SWcs) feedbacks on the $\hat{h}_n$ variance (in day^{-1}) for the first 30 days of the 295 K simulation and ranked according to the column relative humidity CRH. Feedbacks are normalized at each time step by the corresponding spatial variance of $\hat{h}_n$. The advection feedback is calculated using hourly model outputs. The black and grey solid lines indicate the time evolution of $\hat{h}_n$ variance (in 10^{-3}, see upper x-axis for its scale) and the CRH rank corresponding to CRH$_c$, respectively.

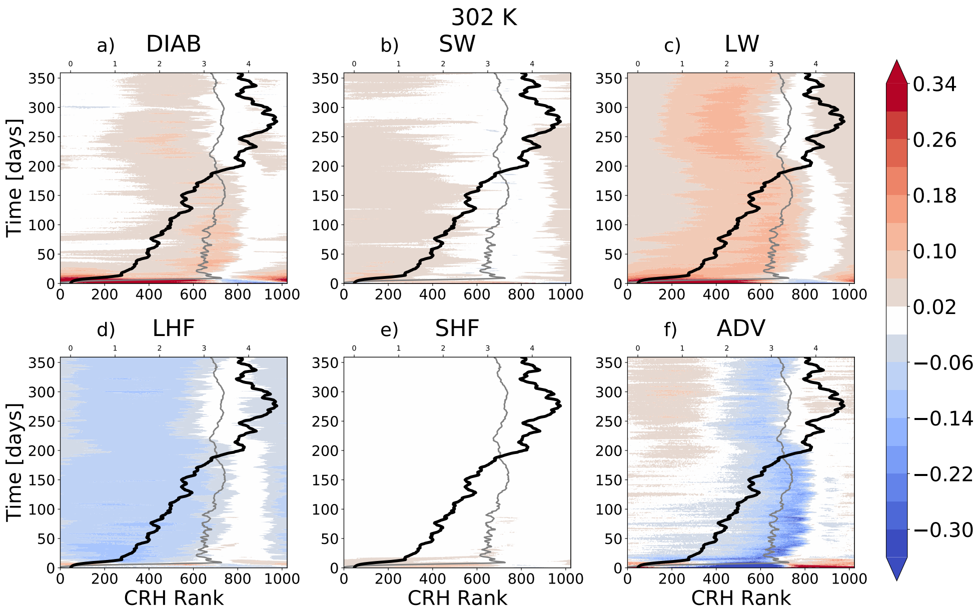

Figure S9. Same as Figure 12 (or S6 or S7) but for the first 360 days of the 302-K simulation.